Effects of the Hydrous Domain in the Mantle Wedge on Magma Formation and Mixing at the Northeast Lau Spreading Center, SW Pacific

Haase, K. M.

2022-03

Haase , K M , Schoenhofen , M V , Storch , B , Beier , C , Regelous , M , Rubin , K & Brandl , P A 2022 , ' Effects of the Hydrous Domain in the Mantle Wedge on Magma Formation and Mixing at the Northeast Lau Spreading Center, SW Pacific ' , Geochemistry, geophysics, geosystems G³. , vol. 23 , no. 3 , e2021GC010066 . https://doi.org/10.1029/2021GC010066

http://hdl.handle.net/10138/342790
https://doi.org/10.1029/2021GC010066

Geochemistry, Geophysics, Geosystems®

RESEARCH ARTICLE
10.1029/2021GC010066

Key Points:

- Variably enriched mantle sources melt beneath the Northeast Lau Spreading Center (NELSC) but there is no evidence for Samoa mantle plume inflow
- Relatively dry fertile mantle beneath NELSC causes sharp geochemical boundary with hydrous harzburgitic North Tonga mantle wedge
- Subducted Louisville Seamount Chain material affects rear-arc volcanism

Supporting Information:

Supporting Information may be found in the online version of this article.

Correspondence to:

K. M. Haase,
karsten.haase@fau.de

Citation:

Haase, K. M., Schoenhofen, M. V., Storch, B., Beier, C., Regelous, M., Rubin, K., & Brandl, P. A. (2022). Effects of the hydrous domain in the mantle wedge on magma formation and mixing at the Northeast Lau Spreading Center, SW Pacific. *Geochemistry, Geophysics, Geosystems*, *23*, e2021GC010066. https://doi.org/10.1029/2021GC010066

Received 27 JUL 2021
Accepted 2 FEB 2022

Author Contributions:

Conceptualization: K. M. Haase, C. Beier, K. Rubin
Funding acquisition: K. M. Haase
Investigation: M. V. Schoenhofen, B. Storch, C. Beier, M. Regelous, K. Rubin, P. A. Brandl
Methodology: K. M. Haase, M. V. Schoenhofen, B. Storch, M. Regelous, K. Rubin, P. A. Brandl
Project Administration: K. M. Haase
Resources: K. M. Haase, M. Regelous, P. A. Brandl

Effects of the Hydrous Domain in the Mantle Wedge on Magma Formation and Mixing at the Northeast Lau Spreading Center, SW Pacific

K. M. Haase[1], M. V. Schoenhofen[1,2], B. Storch[1], C. Beier[1,3], M. Regelous[1], K. Rubin[4], and P. A. Brandl[5]

[1]GeoZentrum Nordbayern, Friedrich-Alexander-Universität (FAU) Erlangen-Nürnberg, Erlangen, Germany, [2]Department of Earth and Planetary Sciences, Macquarie University, Sydney, NSW, Australia, [3]Department of Geosciences and Geography, University of Helsinki, Helsinki, Finland, [4]School of Ocean and Earth Science and Technology, University of Hawaii at Manoa, Honolulu, HI, USA, [5]GEOMAR Helmholtz Centre for Ocean Research Kiel, Kiel, Germany

Abstract Abundant volcanic activity occurs in the back-arc region of the northern Tofua island arc where the Northeast Lau Spreading Center (NELSC) propagates southwards into older crust causing the formation of numerous seamounts at the propagating rift tip. An off-axis volcanic diagonal ridge (DR) occurs at the eastern flank of the NELSC, linking the large rear-arc volcano Niuatahi with the NELSC. New geochemical data from the NELSC, the southern propagator seamounts, and DR reveal that the NELSC lavas are tholeiitic basalts whereas the rear-arc volcanoes typically erupt lavas with boninitic composition. The sharp geochemical boundary probably reflects the viscosity contrast between off-axis hydrous harzburgitic mantle and dry fertile mantle beneath the NELSC. The new data do not indicate an inflow of Samoa plume mantle into the NELSC, confirming previously published He isotope data. The NELSC magmas form by mixing of an enriched and a depleted Indian Ocean-type upper mantle end-member implying a highly heterogeneous upper mantle composition in this area. Most NELSC lavas are little affected by a slab component implying that melting is adiabatic beneath the spreading center. The DR lavas show the influence of a component from the subducted Louisville Seamount Chain, which was previously thought to be restricted to the nearby arc volcanoes Niuatoputapu and Tafahi. This signature is rarely detected along the NELSC implying little mixing of melts from the low-viscosity hydrous portion of the mantle wedge beneath the rear-arc volcanoes into the melting region of the dry mantle beneath the NELSC.

Plain Language Summary Volcanic activity is abundant at subduction zones and the chemical analysis of the erupted rocks allows to determine the material transport in the Earth's mantle. The Northeast Lau Spreading Center (NELSC) forms by extension and volcanism behind the northern Tofua island arc. Several large volcanic structures occur east of the NELSC and the lavas of these off-axis volcanoes are chemically and isotopically distinct implying little mixing with the magmas of the NELSC. The differences suggest decompression melting of relatively dry mantle beneath the NELSC whereas the off-axis volcanoes reflect melting of water-rich mantle affected by fluids from the subducting Pacific Plate. The sharp geochemical boundary between the NELSC and off-axis volcanoes is probably due to a large viscosity contrast between hydrous harzburgitic mantle and dry fertile mantle. Element and isotope ratios indicate that the NELSC magmas form by mixing of enriched and depleted portions of the upper mantle, and we do not find evidence for inflow of the Samoa deep mantle plume from the north. Some of the off-axis lavas contain a component from a volcanic chain that was subducted some 4 million years ago and that was previously only known in two volcanoes of the Tofua island arc.

1. Introduction

Lavas erupted at back-arc spreading centers have variable incompatible element and isotope compositions ranging from depleted normal mid-ocean ridge basalts (N-MORB) to enriched back-arc basin basalts resembling island arc basalts, or more rarely, oceanic intraplate basalts (e.g., Fretzdorff et al., 2002; Pearce & Stern, 2006; Saunders & Tarney, 1984; Volpe et al., 1988). Back-arc magmas typically form by decompression melting depending on the temperature and composition of the mantle, but the influx of volatiles from the subducting slab may lower the solidus causing hydrous melting close to the island arc (Langmuir et al., 2006; B. E. Taylor & Martinez, 2003).

Supervision: K. M. Haase, C. Beier, M. Regelous, K. Rubin, P. A. Brandl
Validation: M. V. Schoenhofen, B. Storch, K. Rubin, P. A. Brandl
Visualization: C. Beier
Writing – original draft: K. M. Haase, M. V. Schoenhofen, B. Storch, C. Beier, M. Regelous, K. Rubin, P. A. Brandl

Thus, the chemical and isotopic compositions of back-arc basin basalts reflect both the mantle flowing from the back-arc region toward the island arc and the flux of components from the subducting slab into the back-arc melting zone (e.g., Hall et al., 2012; Sleeper & Martinez, 2014). The formation of a hydrous domain in the mantle wedge probably has a strong effect on mantle viscosity (Billen & Gurnis, 2001), causing significant changes in magma composition and crustal properties in the back-arc (Dunn & Martinez, 2011; Sleeper & Martinez, 2014). The intensity of the chemical and isotopic influence of components from the subducted slab on back-arc magmas strongly depends on the proximity to the island arc (e.g., Fretzdorff et al., 2002; Harmon & Blackman, 2010; Pearce et al., 1995). Additionally, fluid-mobile elements like Ba and Pb appear to be mobilized and transported differently than Th or La from the slab to the back-arc melting region (Pearce et al., 2005). Partial melting beneath the back-arc rift causes depletion of the upper mantle flowing toward the island arc, particularly in incompatible elements (McCulloch & Gamble, 1991; Woodhead et al., 1993).

The northern Lau Basin behind the northernmost Tofua island arc (Figure 1) is a highly complex back-arc region with several spreading axes that are caused by the very fast subduction and slab rollback of the subducting Pacific Plate (Baxter et al., 2020; Pelletier et al., 1998; Zellmer & Taylor, 2001). The fast back-arc extension in the northern Lau Basin probably started at ∼5.5 Ma as a result of subduction of the Louisville Seamount Chain beneath northern Tonga (Ruellan et al., 2003). Additionally, the northern Lau Basin is probably affected by southward-directed inflow of hot mantle plume material from the Samoa Hotspot (Figure 1), which is indicated by high $^{3}He/^{4}He > 9$ R/Ra observed in lavas and hydrothermal vent fluids (e.g., Lupton et al., 2015; Poreda & Craig, 1992; S. Turner & Hawkesworth, 1998), and which had also been suggested based on tectonic considerations (Danyushevsky et al., 1995). The different components affecting the upper mantle beneath the northern Lau Basin and the abundance of young volcanism allow to trace the transport and mixing processes.

Here, we present major and trace element as well as radiogenic isotope compositions of fresh volcanic glasses and whole rocks along the axis of the Northeast Lau Spreading Center (NELSC) as well as off-axis volcanoes. We find that three components contribute to the magmas, two of which reside in the upper mantle, whereas the third originates from the subducting slab. An incompatible element-enriched component in the upper mantle shows distinct isotope compositions and apparently is not the result of inflow of Samoa plume material. Rather, this enriched component may reside in the upper mantle. The highly variable isotope and incompatible element composition of the NELSC and off-axis lavas suggests a heterogeneous mantle and the ascent of fertile mantle along the NELSC. In contrast, the lavas erupting on the Tonga Microplate to the east of the NELSC all form from a harzburgitic mantle that is re-enriched by slab components, implying a strong effect of the hydrous mantle wedge domain on magma formation and mantle dynamics.

2. Geological Setting

The Tonga-Kermadec subduction system is located in the SW Pacific north of New Zealand where the Pacific Plate is subducting underneath the Indo-Australian Plate. The active arc has a length of ∼2,800 km, with the Tofua island arc extending some 1,200 km north of the intersection with the Louisville Seamount Chain at ∼26°S. Several spreading axes exist in the Lau back-arc basins with the NELSC forming the northern extension of the Fonualei Spreading Center (FSC) and Mangatolu (King's) Triple Junction (MTJ; Figure 1a). The NELSC and FSC form the boundary between the Tonga and the Niuafo'ou microplates (Baxter et al., 2020; Pelletier et al., 1998; Zellmer & Taylor, 2001). The Lau Basin started opening 5.5 to 6 Ma ago due to the southwards directed sweeping of the Louisville Seamount Chain along the Tofua island arc (Pelletier et al., 1998; Ruellan et al., 2003; Zellmer & Taylor, 2001). The subduction rate increases northwards from 164 mm/yr in the central Tofua island arc up to 240 mm/yr in the northern Tofua island arc, causing fast opening rates of 159 mm/yr in the northern Lau Basin (Bevis et al., 1995). The spreading rates at the NELSC and MTJ appear to decrease from 42 mm/yr in the north to 30 mm/yr in the south (Baker et al., 2019). The Vitiaz Fracture Zone terminates the Lau Basin in the north (Figure 1) and the Tonga Trench in the east and northeast as the Pacific Plate bends at the northern end of the subduction zone forming a transition from convergent to transform plate boundary (Bonnardot et al., 2007; Millen & Hamburger, 1998).

Few active volcanoes occur in the arc front of the northern Tonga region and it was suggested that the FSC captured the slab flux leading to a volcanic shut down of the adjacent arc (Escrig et al., 2012; Keller et al., 2008). The young volcanic islands of Tafahi and Niuatoputapu occur east of the overlap region between the NELSC and

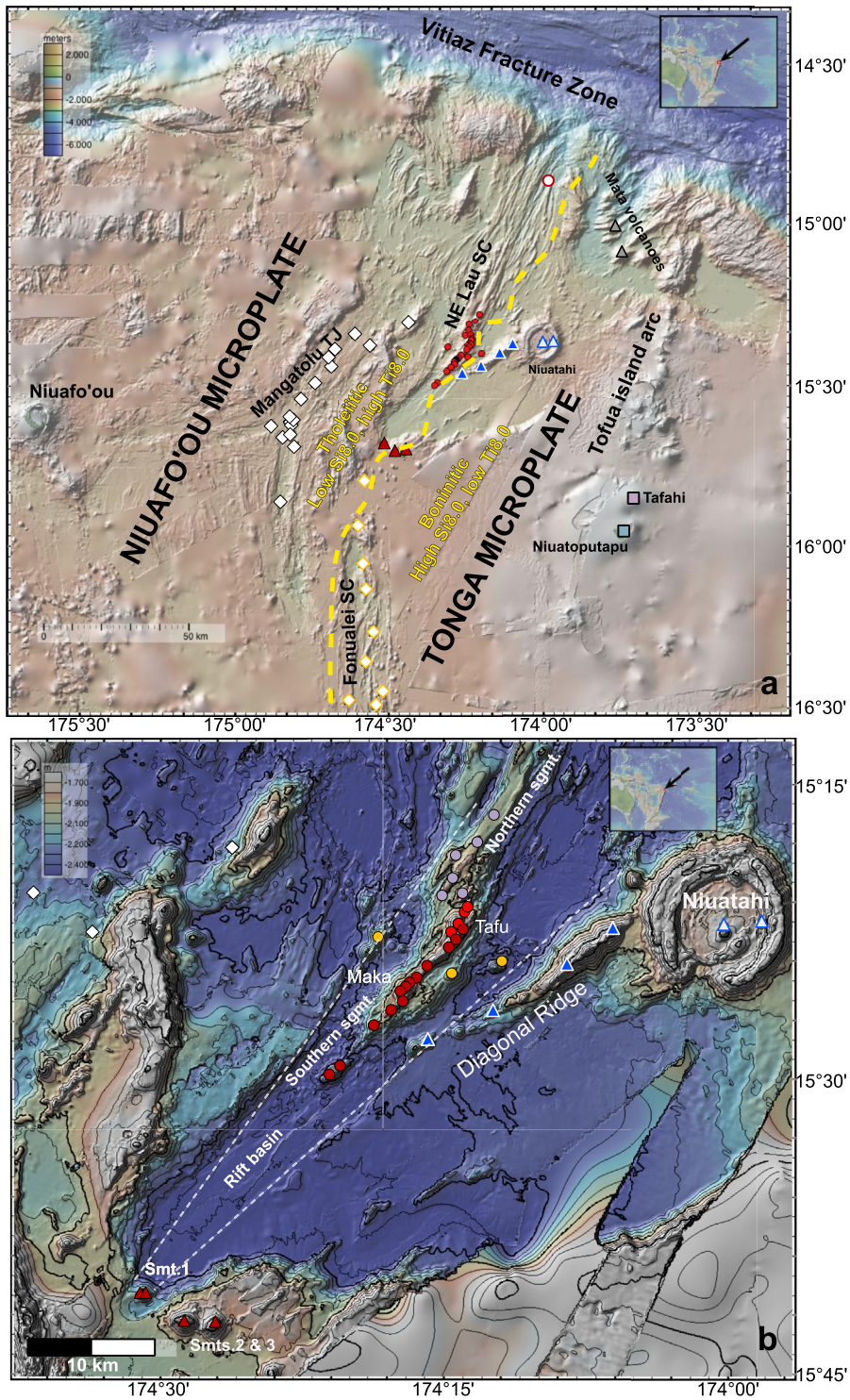

Figure 1. Overview map of the working area showing (a) the northern Tonga Ridge and Lau Basin with the Northeast Lau Spreading Center (NELSC), diagonal ridge (DR), Niuatahi Volcano, the Magatolu Triple Junction (MTJ), and Fonualei Spreading Center (FSC). The symbols show the locations of samples from the SO263 cruise from this study (NELSC: red circles and DR: blue triangles with white rim), and those of previous work on NELSC (white circle with red rim), Mata (gray triangles) and Niuatahi (white triangle with blue rim) volcanoes (Falloon et al., 2007; Park et al., 2015; Resing et al., 2011), as well as the MTJ (diamonds with black rims) and FSC (diamonds with yellow rims) (Caulfield et al., 2012; Danyushevsky et al., 1993; Escrig et al., 2012; Keller et al., 2008; Tian et al., 2011; Volpe et al., 1988). The yellow dashed line shows the location of the boundary between the western dry mantle and the eastern hydrous mantle. (b) Enlarged bathymetric map of the NELSC and Niuatahi Volcano with the sample locations from the SO263 cruise. Note the gap in volcanic structures between the NELSC and the seamounts at the southern rift tip. Maps prepared with GeoMapApp http://www.geomapapp.org.

FSC and erupt lavas suggesting melting of harzburgitic mantle, but isotope ratios implying influence by a component from the subducted Louisville Seamount Chain (Beier et al., 2017; Ewart et al., 1998; Regelous et al., 1997; S. Turner et al., 1997). The composition of the mantle underneath northern Lau Basin has Indian MORB isotopic signatures, and is flowing southwards replacing Pacific-type upper mantle (Hergt & Hawkesworth, 1994; Pearce et al., 2007) and seismic data suggest elevated upper mantle temperatures beneath the NELSC (Wiens et al., 2006). Enriched Samoan plume mantle flows into the NW Lau Basin from the north causing high $^{3}He/^{4}He$ ratios >9 R/Ra (Lupton et al., 2009; Poreda & Craig, 1992; S. Turner & Hawkesworth, 1998) and the incompatible element enrichment and isotope composition of many lavas from the NE Lau Basin possibly also reflects the contribution of Samoan plume mantle (Danyushevsky et al., 1995; Falloon et al., 2007; Pearce et al., 2007; Price et al., 2014; Volpe et al., 1988). Additionally, another enriched mantle source may have contributed to magmas in the northern Tonga island arc region (Danyushevsky et al., 1995; Falloon & Crawford, 1991), and was suggested to be related to the HIMU-type mantle source of the Cook-Austral volcanic chain, either from mantle inflow (Falloon et al., 2007) or from subducting material (Price et al., 2016). However, the He isotope ratios of the NELSC lavas as well as those from the MTJ are typical for upper mantle values, indicating that Samoan mantle did not affect this region widely (Lupton et al., 2009, 2015; Tian et al., 2011). Many FSC lavas have a boninitic signature which was explained by a combination of large subduction input, extreme mantle depletion, and high total degrees of partial melting up to 38% (Escrig et al., 2012; Keller et al., 2008). The NE Lau Basin has long been known for the abundance of boninitic lavas, that is, mafic rocks with relatively high SiO_2 and low TiO_2 contents that were sampled in the fore-arc and rear-arc (Danyushevsky et al., 1995; Falloon et al., 2007; Resing et al., 2011; Sharaskin et al., 1983).

The NELSC lies some 70 km west of the northern Tofua island arc and consists of several overlapping volcanic ridges up to 20 km in length and 1 km in width that are situated in an ~20 km wide NE-SW-striking rift basin (Figure 1b). The shallowest volcanoes were named Tafu with a summit at 1,369 mbsl and Maka at 1,524 mbsl water depth compared to a depth of ~2,600 mbsl for the surrounding basin (Baker et al., 2011). Several off-axis seamounts occur in the region as well as ridges that probably formed by rifting at the spreading axis. The southernmost volcanic ridge structure of the NELSC occurs at 15°30′S, but the bathymetry of the V-shaped basin indicates that the tip of the NELSC propagates ~30 km to the south into older crust (Figure 1b). This segment of the rift basin is flat and sediment-covered without any evidence for volcanic activity. A volcanic cone (Seamount 1) occurs within the rift tip in older crust and several seamounts (Seamounts 2 and 3) are located on the southern flank of the rift (Figure 1b). The northern rift tip of the FSC lies some 30 km to the south of the NELSC, but there are several volcanic cones on the old crust between the NELSC and FSC rifts (Figure 1a) suggesting the two rifts may try to link (Baxter et al., 2020). The spreading axis of the MTJ occurs ~35 km to the west and overlaps with both the NELSC and FSC (Figure 1a). Water depths range from 1,259 mbsl at the southernmost seamounts to 2,280 mbsl at the southern part of the NELSC. In general, the NELSC ranges from 1,400 to 1,900 mbsl water depth, while the off-axis samples were sampled at water depths of up to 2,130 mbsl. The large Niuatahi volcano (formerly Volcano O) lies some 15 km east of the NELSC (Figure 1) and is connected to the southern NELSC by the SW-NE striking diagonal ridge (DR; Park et al., 2015). Niuatahi has a large caldera with a diameter of 8 km, a young volcanic cone in the caldera (Kim et al., 2011), and is surrounded by ~166 km^2 of dacitic lava flows (Embley & Rubin, 2018).

3. Sampling and Methods

Here, we present geochemical data on new rock samples from the NELSC and the DR that were recovered during RV Sonne cruise SO263 TongaRift in July 2018. Five samples from the DR were recovered by TV-guided grab from the GEOMAR Helmholtz Zentrum für Ozeanforschung Kiel (TVG). Forty-seven samples from the NELSC including some from the Maka volcano were taken by wax-corer and ROV MARUM QUEST. Several off-axis seamounts and three volcanoes at the southern tip of the NELSC (Seamounts 1–3) were also sampled using the TVG (Figure 1). We analyzed 57 samples from the vicinity of the NELSC, six of which are whole rocks from the southern seamounts (Figure 1) and the remaining samples are fresh volcanic glasses ($n = 51$). The data as well as analyses of rock standards analyzed together with the samples are presented in Table S1.

In samples with fresh volcanic glass, major element contents were measured with a JEOL JXA 8200 Superprobe electron microprobe at the GeoZentrum Nordbayern (GZN), Friedrich-Alexander-Universität (FAU) Erlangen-Nürnberg. The instrument was operated using an acceleration voltage of 15 kV, a beam current of 15 nA,

and a beam diameter of 10 µm following the methods outlined by Brandl et al. (2012) and Beier et al. (2018). Accuracy and precision of the analyses were determined by repeated (n = 34) measurement of glass standard USNM 111240/52 VG-2 (Jarosevich et al., 1980). The accuracy and precision are generally better than 3% with the exception of MnO, MgO, and P_2O_5 which are better than 5%. Chlorine and S concentrations in standard VG-2 yielded 280 and 1,438 ppm (Table S1), respectively, which is comparable to the contents of 297 and 1,441 ppm published by de Hoog et al. (2001).

Lavas from the southern seamounts do not contain glass and thus, whole rock major and selected trace element compositions were measured with a Spectro XEPOS He X-ray fluorescence spectrometer at the GZN, FAU Erlangen-Nürnberg using methods described previously (Freund et al., 2014). Accuracy and precision of the measurements were determined by multiple measurements of international rock standards BE-N and GA. The accuracy is generally better than 5% with the exception of P_2O_5, where it is better than 10%. The precision is better than 2%. Whole rock samples from the NELSC have a loss of ignition (LOI) of <0.03 wt.%, but some DR samples show elevated values up to 5.22 wt.% probably due to seawater alteration.

Water concentrations of NELSC and DR glass rims were determined at the Australian National University (ANU), Canberra, Australia on the sensitive high-resolution ion microprobe—stable isotope (SHRIMP-SI). The handpicked glass chips were embedded in synthetic resin, polished and carefully removed from the resin by acetone and a hand-drill to embed the polished samples into aluminum holders in In. The mounts were coated with Au and analyzed for $^{16}O^-$ and $^{16}O^1H^-$ with the method described in M. Turner et al. (2015) finding measurement spots avoiding cracks and inclusions in the glasses. Internal basaltic glass standards ND61, ND70 and 24.1 (M. Turner et al., 2015) were used to determine the reproducibility and accuracy. The sample water data (Table S1) were calculated by the sensitivity factor given by the standard analyses and the sample measurements.

Trace elements on the volcanic glasses were measured by laser ablation ICP-MS at the GZN using an Analyte Excite 193nm laser (Teledyne Photon Machines) coupled to an Agilent 7500c ICP-MS at the GZN, FAU Erlangen-Nürnberg. Repeated analyses of the basaltic rock standard BCR-2G (n = 3) give an accuracy of <10% for all elements (except Li < 14% and Zn < 35%), and a reproducibility of <6% for all elements (except for As, Yb < 7%; Li, Ag, Ta, Bi < 12%). Trace elements of whole rock powders were analyzed by solution ICP-MS at the GZN using a Thermo Fisher Scientific XSeries 2 Quadrupole ICP-MS connected to an Aridus 2 membrane desolvating sample introduction system. Repeated measurements of the international rock standards BHVO-2 give a precision and accuracy better than 1.1% (2σ) and 1.1% (2σ), respectively.

Selected samples from the different settings were processed and measured for their Sr-Nd-Hf-Pb isotope ratios at the GZN, FAU Erlangen-Nürnberg, following the methods described in Romer et al. (2019) and Storch et al. (2020). The whole rock powder (126-01, 126-02, 124-02) and volcanic glass chips were leached beforehand, with 6M HCl for 2h or with a mixture of 2.5M HCl + H_2O_2 + MQ H_2O (mixing ratio 1:1:2) for 10 min, respectively. The samples were washed two times with MQ H2O and dried at 70°C overnight. The Sr and Nd isotope compositions were analyzed using a Thermo Fisher Triton Series Thermal Ionization Mass Spectrometer in static mode. The Hf isotopes and double spiked Pb isotope ratios were determined using a Thermo Fisher Neptune Plus High Resolution Multicollector ICP-MS in static mode. Strontium isotope measurements were corrected for mass fractionation using an exponential fractionation law with $^{88}Sr/^{86}Sr = 0.1194$ with mass 85 to correct the contribution of ^{87}Rb to ^{87}Sr. Neodymium isotope data were corrected for mass fractionation using $^{146}Nd/^{144}Nd = 0.7219$, and Hf isotope ratios assuming $^{179}Hf/^{177}Hf = 0.7325$, both assuming an exponential fractionation law. The standard NBS987 measurements (n = 3) show $^{87}Sr/^{86}Sr = 0.710270 \pm 0.000005$ (2σ), and the Erlangen Nd standard (n = 10) gave $^{143}Nd/^{144}Nd = 0.511538 \pm 0.000005$ (2σ; see Table S1). Three measurements of Nd isotope ratios for the La Jolla Nd isotope standard yielded an average of 0.511850 ± 0.000015 (2σ), similar within error to the suggested value of 0.511856 ± 0.000008 (2σ; Thirlwall, 1991), so that data were not corrected. The Sr isotope compositions of the samples were corrected to the NBS987 = 0.710250. Our measurements of the Grenoble Hf isotope standard together with the samples yielded an average composition (n = 3) of 0.282157 ± 0.000010 (2σ) and the measured isotope compositions were corrected to an average value for the AMES Grenoble Hf standard of 0.282166 (n = 36). Chauvel et al. (2011) gave a reference value for the AMES Grenoble $^{176}Hf/^{177}Hf$ of 0.282160, which is comparable to the results for the JMC 475 standard ($^{176}Hf/^{177}Hf = 0.282160$) from Vervoort and Blichert-Toft (1999). The international rock standard BHVO-2 analyzed with the samples yielded 0.283108 ± 0.000002 (2σ), in agreement with published values of 0.283098 ± 0.000011 (2σ) and 0.283106 ± 0.000011 (2σ), respectively

(Chauvel et al., 2011). Negligible blanks of 110 pg Sr, 20 pg Hf, and 15 pg Nd were determined for the dissolution and separation chemistry.

Lead isotope measurements were carried out using a ^{207}Pb-^{204}Pb double spike to correct for instrumental mass fractionation. The double spike, with a $^{207}Pb/^{204}Pb$ ratio of 0.813508 was calibrated against a solution of the NBS982 equal atom Pb standard, and yielded $^{206}Pb/^{204}Pb$, $^{207}Pb/^{204}Pb$ and $^{208}Pb/^{204}Pb$ ratios of 16.9410 ± 0.0019, 15.4993 ± 0.0018 and 36.7244 ± 0.0042 for the NBS981 standard measured as an unknown. These values are comparable within error to those obtained using the double- or triple-spike method in other laboratories (R. N. Taylor et al., 2015). Lead samples were diluted with 2% HNO_3 to a concentration of about 20 ppb, and an aliquot of this solution spiked in order to obtain a $^{208}Pb/^{204}Pb$ ratio of about 1. Spiked and unspiked sample solutions were introduced into the plasma via Cetac Aridus desolvating nebulizer, and measured in static mode. Interference of ^{204}Hg on mass 204 was corrected by monitoring ^{202}Hg, but was usually negligible. An exponential fractionation correction was applied offline using the iterative method of Compston and Oversby (1969). Four measurements of the NBS981 standard were measured together with each batch of 10 samples, and the mean measured $^{206}Pb/^{204}Pb$, $^{207}Pb/^{204}Pb$, and $^{208}Pb/^{204}Pb$ ratios for NBS981 during that run were used to normalize sample data using the standard values above. Measurement of the international rock standard BHVO-2 yielded $^{206}Pb/^{204}Pb$, $^{207}Pb/^{204}Pb$, and $^{208}Pb/^{204}Pb$ of 18.6943 ± 0.0002 (2σ), 15.5408 ± 0.0002 (2σ), and 38.2622 ± 0.0006 (2σ), respectively, which is slightly higher than the ratios 18.6474 ± 0.0242 (2σ), 15.5334 ± 0.0094 (2σ), and 38.2367 ± 0.0182 (2σ) provided by Weis et al. (2006). However, the BHVO-2 was shown to be heterogeneous in Pb isotopic composition, probably due to contamination during standard preparation, and some of the leachates of this standard yielded high Pb isotope ratios similar to our results (Weis et al., 2005). Lead blanks are <40 pg.

4. Results

4.1. Petrographic Description of the Samples

The ROV and TV-grab samples from the NELSC are generally aphyric to plagioclase-olivine-clinopyroxene-microphyric pillow lavas with up to 10 mm thick fresh glass rims and thin Mn-Fe oxide coatings. The size of the microphenocrysts is typically less than 1 mm and all samples are highly vesicular with up to 40% vesicles. Rarely, highly porphyritic lavas with phenocrysts of plagioclase, clinopyroxene, and occasionally olivine to 4 mm size were sampled (e.g., 117TVG-01). The samples from the off-axis seamounts (~1.6–4.7 km distant from the NELSC) are highly vesicular lavas with glass rims and thin Mn-Fe oxide coating or glass fragments. Some of the off-axis seamount lavas contain microphenocrysts of olivine, plagioclase, and clinopyroxene. The lava samples from the Seamounts 1–3 are porphyritic with up to 60% vesicles. Plagioclase (<2 mm) and clinopyroxene are common (<4 mm), whereas olivine crystals are rare except for one picritic sample from Seamount 1 (SO263 124TVG-03) with ~30% olivine phenocrysts. Two basalt samples have glass rims thick enough for geochemical analysis. Most samples from the DR are plagioclase-clinopyroxene-porphyritic lavas with up to 15% vesicles and thin coatings of Mn-oxide-hydroxides. Few samples have glass rims and phenocrysts are typically smaller than 2 mm. Additionally, three fresh pumice samples containing phenocrysts of plagioclase and clinopyroxene were sampled on the DR.

4.2. Chemical Compositions of the Lavas

The glass samples from the NELSC with >6 wt.% MgO have SiO_2 < 50 wt.% (Figure 2), that is, they are basaltic in composition whereas the more evolved lavas are basaltic andesites. Samples from the NELSC range from 3.8 to 9.0 wt.% MgO (Figure 2) and all NELSC samples broadly display comparable trends in their major elements. In contrast to the basaltic NELSC samples, the eight glass samples and seven whole rock samples from the DR range from basaltic andesite to dacite in composition. The data show two trends: (a) a typical tholeiitic trend of increasing FeO^T and TiO_2 with decreasing MgO followed by the NELSC as well as those from the MTJ and FSC and (b) a calc-alkaline-like trend with an early decrease in FeO^T and relatively constant TiO_2 contents followed by the off-axis lavas of the DR and Niuatahi volcano. The latter samples have higher SiO_2 and lower TiO_2, and Na_2O contents at a given MgO (Figure 2). The primitive DR rocks with 13–14 wt.% MgO and <0.5 wt.% TiO_2 have SiO_2 contents >52 wt.% and thus classify as boninites (Le Bas, 2000) similar to lavas from the Mata volcanoes (Resing et al., 2011). The DR samples as well as those from Niuatahi volcano generally have TiO_2 concentrations <0.7 wt.% with constant TiO_2 and FeO^T at variable MgO resembling lavas from the arc front volcanoes of Tafahi

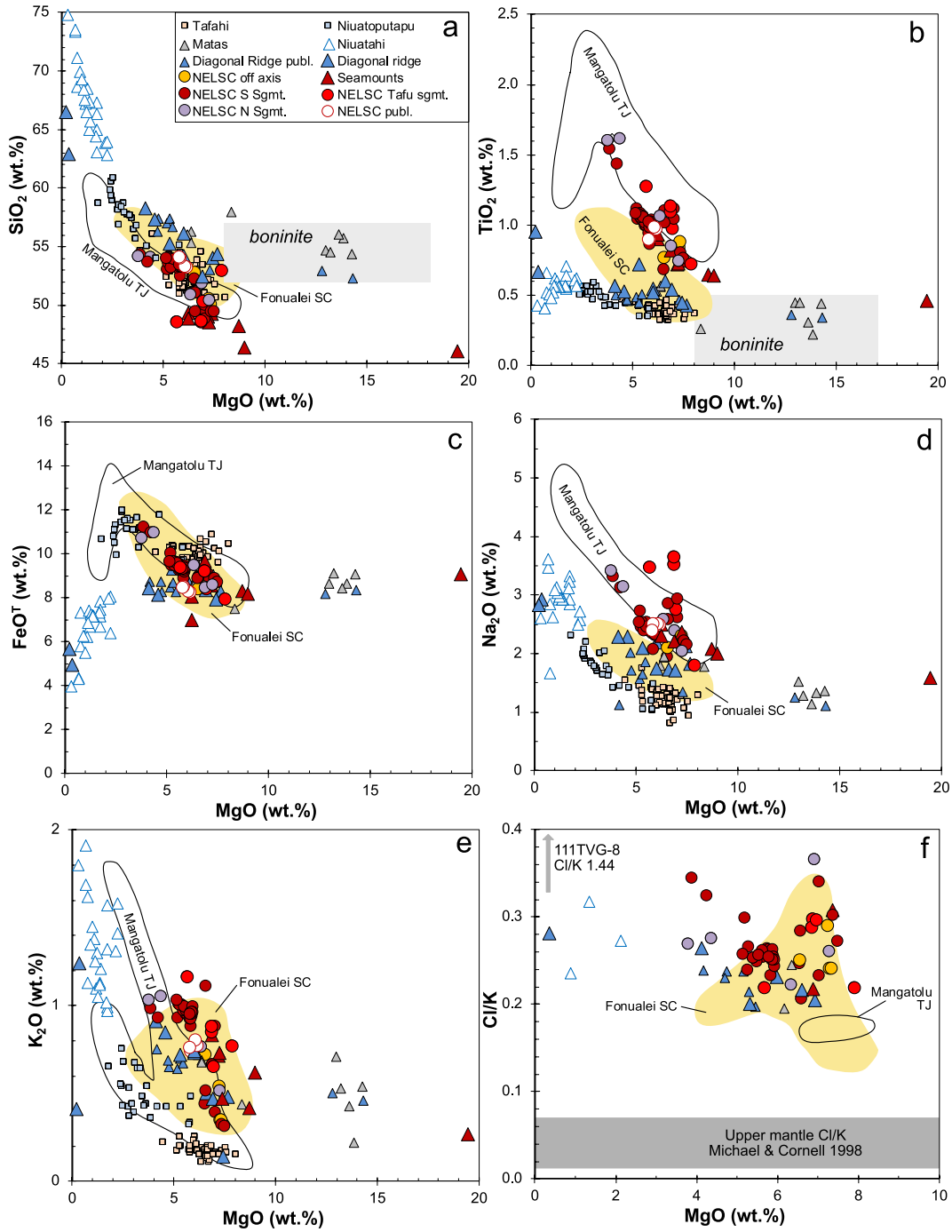

Figure 2. Selected major element concentrations of (a) SiO_2, (b) TiO_2, (c) FeO^T, (d) Na_2O, (e) K_2O, and (f) Cl/K versus MgO (wt.%). Literature data for the diagonal ridge (Falloon et al., 2007; Park et al., 2015), Niuatahi Volcano (Falloon et al., 2007; Park et al., 2015), Mangatolu Triple Junction, and Foundation Spreading Center (Caulfield et al., 2012; Danyushevsky et al., 1993; Escrig et al., 2012; Keller et al., 2008; Tian et al., 2011; Volpe et al., 1988).

and Niuatoputapu (Figure 2b). The mafic samples have similar FeO^T compared to those of the NELSC, but the more evolved DR rocks lie on a decreasing FeO^T trend with decreasing MgO (Figure 2c). The K_2O contents the DR lavas overlap with the NELSC samples but are relatively low compared to the lavas from the axis (Figure 2c). The Cl/K ratios of the glasses range from 0.13 to 0.37 similar to the variation observed in FSC glasses (Figure 2f) and only sample 111TVG-08 has an elevated ratio of 1.44 probably indicating seawater alteration. We do not

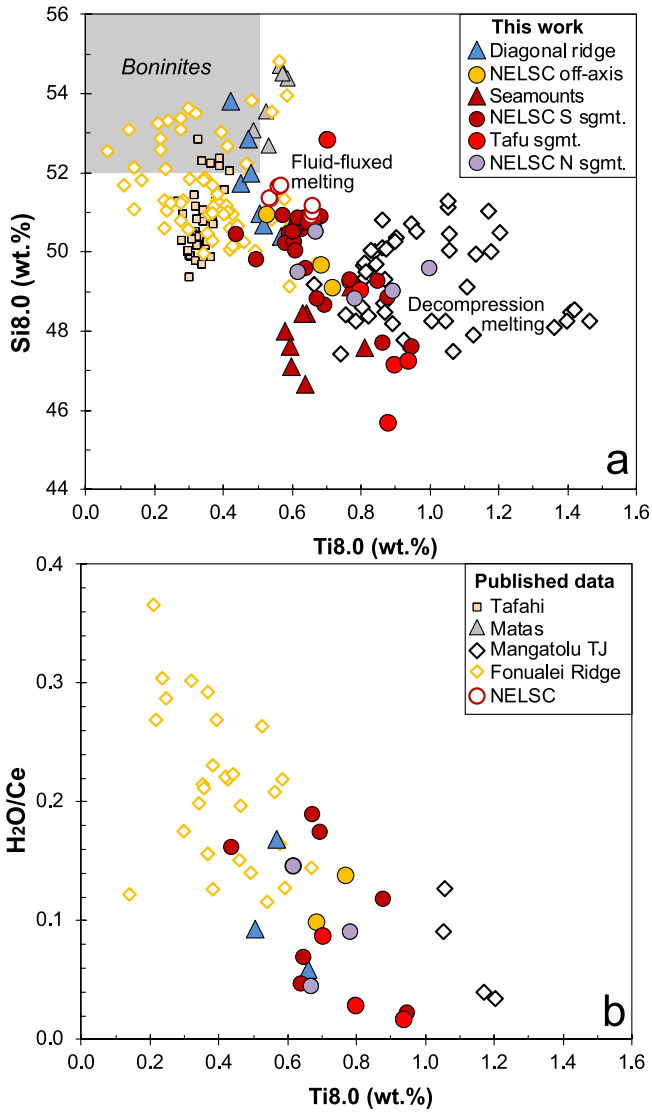

Figure 3. (a) Fractionation-corrected SiO_2 (Si8.0) versus TiO_2 (Ti8.0) concentrations for the Northeast Lau Spreading Center (NELSC) lavas in comparison to lavas from the diagonal ridge, the Mata volcanoes, Fonualei Spreading Center (FSC), and Magatolu Triple Junction (MTJ). (b) The ratio of H_2O/Ce versus the fractionation-corrected TiO_2 content showing a rough negative trend. The correction of SiO_2 and TiO_2 is recalculated to 8 wt.% MgO using the following equations (derived from trends in Figure 2) for the NELSC, MTJ, and FSC lavas between 8 and 3 wt.%: Si8.0 = SiO_2 − 1.23 (8 − MgO) and for the other lavas Si8.0 = SiO_2 − 1.62 (8 − MgO). The NELSC, MTJ, and FSC lavas between 8 and 3 wt.% were corrected using: Ti8.0 = TiO_2 − 0.168 (8 − MgO) and for the other lavas Ti8.0 = TiO_2 − 0.023 (8 − MgO). Samples with less than 3 wt.% MgO were not used and samples with >8 wt.% MgO are uncorrected because they lie along olivine control lines with very flat trend. Also shown is the field for the classification of boninites with >8 wt.% MgO, >52 wt.% SiO_2, and <0.5 wt.% TiO_2 (Le Bas, 2000). Data sources as in Figure 2.

find a correlation of Cl/K with element ratios like Ce/Pb, U/Nb, or Ba/La (not shown).

The trends of SiO_2 and TiO_2 with MgO in Figure 2 can be used to determine linear equations for recalculating fractionation-corrected primitive magma compositions at 8 wt.% MgO (Pearce & Reagan, 2019; Pearce & Robinson, 2010). Only lavas with 3–8 wt% MgO are fractionation-corrected by using the equations given in Figure 3, and more evolved samples are not used whereas the SiO_2 and TiO_2 contents of samples with >8 wt.% MgO are not corrected because they lie on flat olivine control lines (Figure 2). It has been shown previously that H_2O is incompatible in the upper mantle resembling Ce in terms of bulk distribution coefficient and thus H_2O/Ce can be used to reflect the H_2O content of the mantle (Michael, 1988). We find rough negative trends of the Si8.0 and H_2O/Ce ratios with Ti8.0 where the DR and Mata off-axis lavas on the Tonga Plate, the FSC lavas as well as the arc front lavas from Tafahi have low Ti8.0 and high Si8.0, resembling boninite (Figure 3). In contrast, the tholeiitic lavas from the NELSC and MTJ have high Ti8.0 and low Si8.0. The FSC lavas also have higher H_2O/Ce and lower Ti8.0 than the NELSC and MZJ basalts, confirming the previously suggested resemblance of FSC lavas to boninite (Escrig et al., 2012).

All lavas from the NELSC, the seamounts, and the DR have lower concentrations of the rare earth elements (REE) and fluid-immobile elements like Nb and Zr compared to depleted MORB (Figure 4). Most samples from the NELSC have slightly enriched light REE relative to the heavy REE (Figure 4), but show depletions of Nb relative to La and very high contents of Sr, Pb, K, and other fluid-mobile elements. In contrast, some lavas from Tafu are enriched in light REE but also have high Nb contents and positive anomalies of Sr and Pb. The lavas from Seamounts 1–3 are variable in incompatible element compositions, for example, having $(La/Sm)_N$ between 1.3 and 1.8. Whereas the basalts from Seamount 1 resemble the NELSC lavas, lavas from Seamount 3 are much more enriched in incompatible elements (e.g., $(La/Sm)_N$ of 1.8) and particularly fluid-mobile elements like Cs, Rb, Ba, and K (Figure 4). The NELSC basalts have $(La/Sm)_N$ between 1.0 and 4.5 and are generally more enriched in light REE than those from the MTJ and FSC (Figures 5 and 6). The variation of incompatible element and isotope ratios is generally larger in the NELSC samples compared to the MTJ and FSC basalts. Gradients from high to low Ba/Nb and low to high Ce/Pb and Nb/La in the lavas exist along the FSC in the south, whereas the NELSC lavas in the north have highly variable compositions (e.g., Ce/Pb 6–15) within a small region (Figure 5). Large variations are also observed in the radiogenic isotope compositions of the NELSC lavas compared to the more restricted compositional ranges of the MTJ and FSC basalts (Figure 5). The Nd isotope ratios also show a gradient of decreasing values from the FSC to the MTJ and the lowest $^{143}Nd/^{144}Nd$ in some NELSC lavas (Figure 5b).

The NELSC lavas generally show higher Nb/Zr than the FSC and MTJ back-arc lavas and the most enriched NELSC lavas have higher Nb/Zr ratios than Samoa (Figure 6). However, the NELSC samples with the lowest Nb/Zr and $(La/Sm)_N$ overlap with lavas from the FSC and MTJ. The NELSC samples have relatively constant U/Nb, Ce/Pb, and Ba/Nb ratios for the large range of Nb/Zr and $(La/Sm)_N$ unlike most FSC basalts that have higher U/Nb and Ba/Nb but lower Nb/Zr and $(La/Sm)_N$. The most enriched NELSC lavas overlap with Samoa lavas in terms of Ba/Nb ~10 and Ce/Pb ~12, but have higher Nb/Zr for a given $(La/Sm)_N$ (Figure 6). The samples from the DR are similar to published data from Niuatahi (Falloon et al., 2007; Park et al., 2015) with

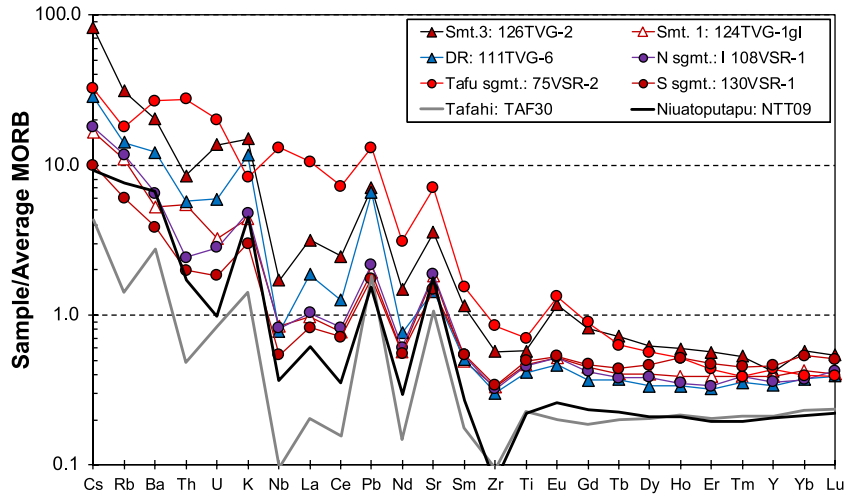

Figure 4. Average-MORB-normalized incompatible element diagram for selected lavas from the Northeast Lau Spreading Center, the southern seamounts, and the off-axis diagonal ridge compared to lavas from Tafahi and Niuatoputapu in the Tonga island arc front (Beier et al., 2017). The MORB average is from Hofmann (1988).

$(La/Sm)_N$ of 2.0–2.5, Ba/Nb of ~40 and Ce/Pb of ~5. For a given $(La/Sm)_N$ the DR lavas have relatively low Nb/Zr compared to the NELSC samples.

Strontium and Nd isotope compositions (Figure 7a) along the NELSC follow a negative trend ranging from 0.70318 to 0.70406 and 0.51275–0.51300, respectively. Basalts from the Tafu segment have the lowest Nd and highest Sr isotope ratios, whereas the lavas from the southern segment and the seamounts overlap with the FSC lavas at relatively low $^{87}Sr/^{86}Sr$ and high $^{143}Nd/^{144}Nd$ isotope ratios. Off-axis lavas and the southernmost seamount samples lie within this range, while DR and Niuatahi samples are displaced to higher Sr isotope ratios at a given Nd isotope ratio of ~0.5129, respectively. The lavas from Samoa have significantly higher Sr isotope ratios than the NELSC lavas at a given $^{143}Nd/^{144}Nd$. The Hf and Nd isotope ratios of the NELSC lavas follow a positive trend within the field of Indian Ocean MORB as defined by Pearce et al. (2007) for the SW Pacific (Figure 7b). Most of the NELSC lavas show positive correlations of $^{206}Pb/^{204}Pb$ isotope ratios with $^{207}Pb/^{204}Pb$ and $^{208}Pb/^{204}Pb$, but there are several samples with $^{206}Pb/^{204}Pb$ of 19.0–19.2, particularly from the region south of the Tafu segment, that deviate toward lower $^{207}Pb/^{204}Pb$ and $^{208}Pb/^{204}Pb$ from this trend (Figure 7d). The NELSC lavas generally lie on a trend of $^{208}Pb/^{204}Pb$ versus $^{206}Pb/^{204}Pb$ that is parallel to the trends of Samoa and Tafahi/Niuatoputapu rocks, but lies between these two trends. The NELSC samples with the least radiogenic Pb isotope ratios from the southern and northern segments overlap with the compositions of the FSC lavas. The DR lavas have the highest $^{206}Pb/^{204}Pb$ ratios but comparably lower $^{207}Pb/^{204}Pb$ and $^{208}Pb/^{204}Pb$, showing a trend of $^{208}Pb/^{204}Pb$ with $^{206}Pb/^{204}Pb$ parallel to that of the NELSC samples. The DR lava compositions resemble those from Tafahi and Niuatoputapu in the northern Tofua island arc. The four NELSC samples deviating from the general trend of the back-arc spreading axis lie between the Pb isotope composition of Tafahi and Niuatoputapu and the NELSC lava trend. There are also rough negative and positive trends between Nd and Sr isotope ratios versus $^{206}Pb/^{204}Pb$, respectively (Figures 7e and 7f), and some lavas show higher $^{87}Sr/^{86}Sr$ deviating from these trends toward the Tafahi and Niuatoputapu compositions.

Incompatible element ratios often form trends with radiogenic isotope compositions and, for example, the Th/Nd of the NELSC lavas lie on a negative trend with $^{143}Nd/^{144}Nd$ (Figure 8a). The $(La/Sm)_N$ ratios vary with $^{206}Pb/^{204}Pb$ showing that the most incompatible element-enriched NELSC lavas from the Tafu segment also have the highest Pb isotope composition, resembling lavas from Samoa (Figure 8b). Several samples with $^{206}Pb/^{204}Pb$ of 19.0–19.2 deviate from the positive trend toward lower $(La/Sm)_N$ and compositions of Tafahi and Niuatoputapu. The lavas with low Pb isotope ratios particularly from the southern and northern NELSC segments and the seamounts have relatively low $(La/Sm)_N$ overlapping with the FSC basalts. The DR samples and the published composition of one Niuatahi lava resemble the Tafahi and Niuatoputapu compositions in terms of isotope and incompatible element ratios. In Ce/Pb versus $^{206}Pb/^{204}Pb$ the NELSC lavas display a rough positive trend with the Tafu samples having the highest Ce/Pb ratios and $^{206}Pb/^{204}Pb$, whereas the samples with $^{206}Pb/^{204}Pb$ of 19.0–19.2 show decreasing

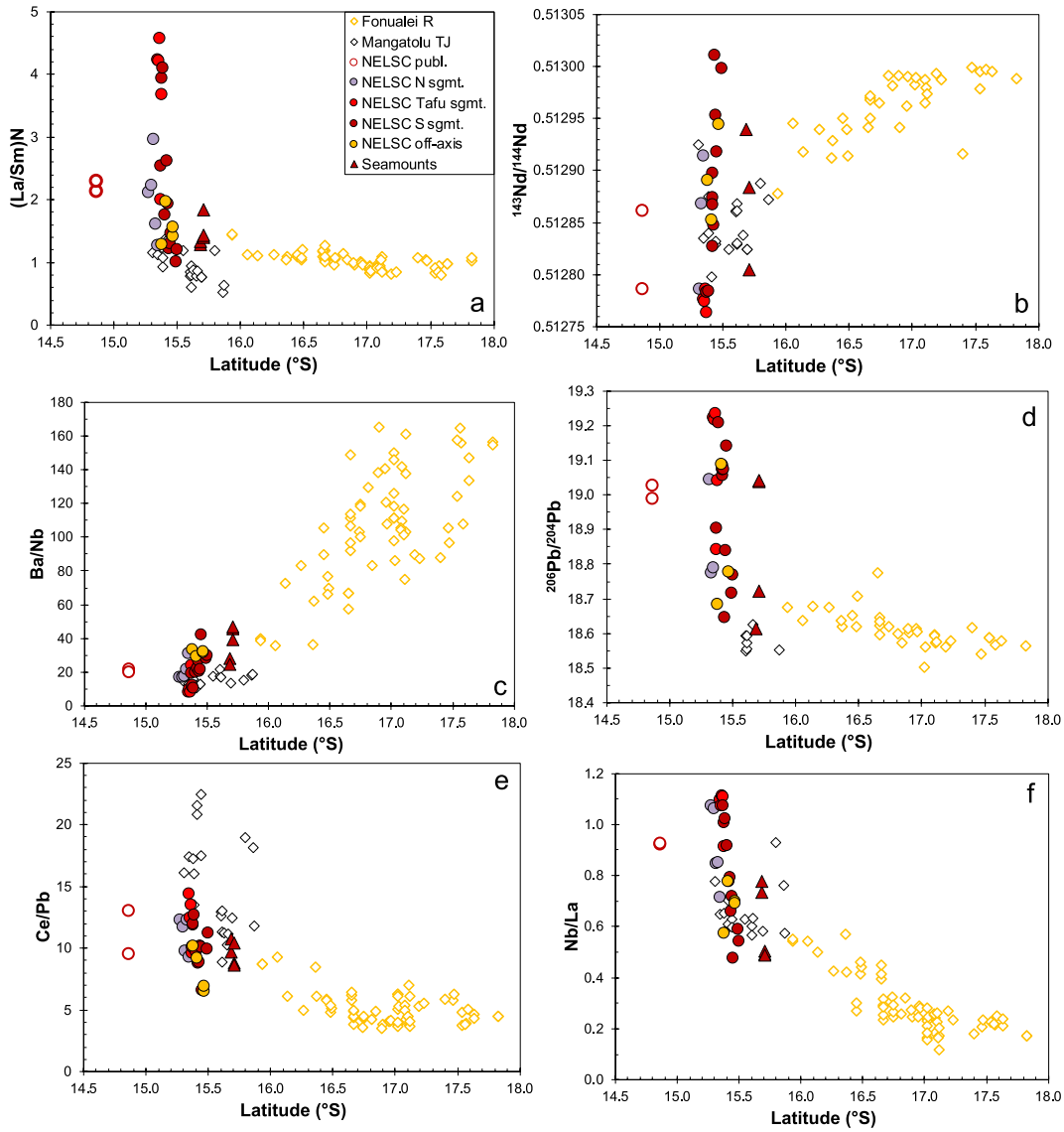

Figure 5. Variation of (a) $(La/Sm)_N$, (b) $^{143}Nd/^{144}Nd$, (c) Ba/Nb, (d) $^{206}Pb/^{204}Pb$, (e) Ce/Pb, and (f) Nb/La versus Latitude along the spreading axes of the Northeast Lau Spreading Center (NELSC), Magatolu Triple Junction, and Fonualei Spreading Center. Note the trends of the different ratios and the large variation at the NELSC. Data sources as in Figure 2 and chondrite for calculation of $(La/Sm)_N$ from Sun and McDonough (1989).

Ce/Pb toward Tafahi and Niuatoputapu compositions (Figure 8c). The Tafu lavas have high Nb/La in contrast to most samples from the southern and northern segments as well as the southern seamounts that overlap with FSC lavas (Figure 8d).

5. Discussion

5.1. Mantle Depletion Beneath the Tonga Plate Inferred From the Variation of TiO_2 Contents in the Northeastern Lau Basin Lavas

Our new data indicate a relatively fertile mantle source beneath the NELSC, because all lavas from the spreading axis as well as those from the seamounts at the propagating tip have relatively high TiO_2 and are tholeiitic basalts to basaltic andesites with relatively low SiO_2 contents (Figure 2). In contrast, lavas and volcanic glasses from the DR have boninitic affinities, that is, the rocks with ~14 wt.% MgO are andesitic with high SiO_2 of 54 wt.%, but the TiO_2 contents are lower than 0.5 wt.% (Figure 2) and thus classify as boninite following the IUGS scheme

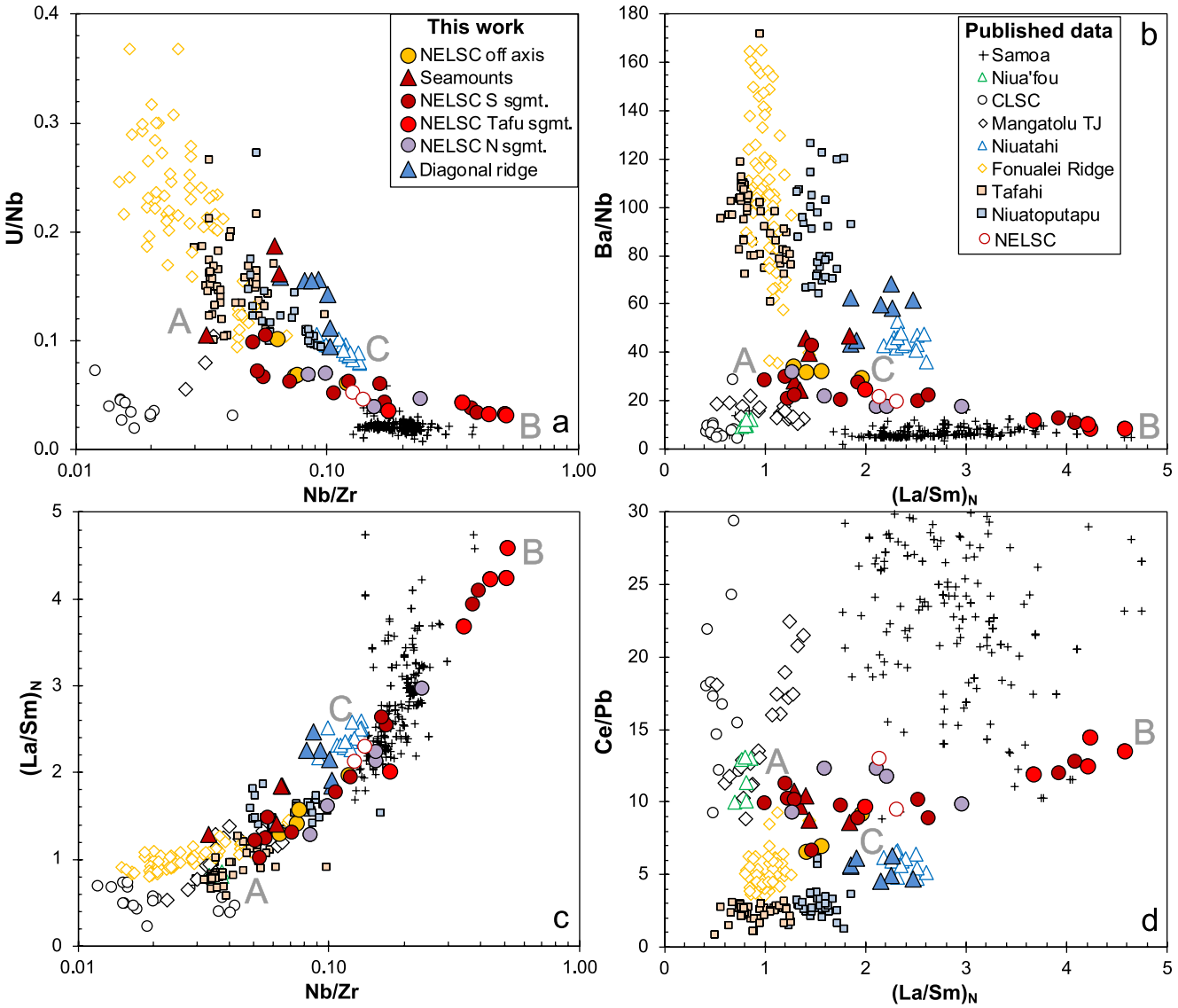

Figure 6. Selected incompatible element ratios of the Northeast Lau Spreading Center and diagonal ridge samples: (a) U/Nb versus Nb/Zr, (b) Ba/Nb versus $(La/Sm)_N$, (c) $(La/Sm)_N$ versus Nb/Zr, and (c) Ce/Pb versus $(La/Sm)_N$ in comparison to Magatolu Triple Junction, Fonualei Spreading Center, and Niuatahi Volcano rocks as well as Samoa hotspot basalts (Jackson et al., 2010; Konter & Jackson, 2012; Palacz & Saunders, 1986; Workman et al., 2004; Wright & White, 1986). Other data sources as in Figure 2.

(Le Bas, 2000). In this respect, the DR lavas resemble the boninites from the Mata rear-arc volcanoes (Figure 1) further to the north (Falloon et al., 2007; Resing et al., 2011). Other primitive magmas forming beneath the Tonga Microplate like those of the Mata volcanoes and those of the FSC also have low TiO_2 contents with a range of 0.4–1.0 wt.% TiO_2 at 8 wt.% MgO (Figure 2). Most of these primitive melts have relatively high SiO_2 contents >52 wt.% with many lavas classifying as boninites (Escrig et al., 2012; Falloon & Crawford, 1991; Falloon et al., 2007; Park et al., 2015; Resing et al., 2011). The DR and Niuatahi lavas with <8 wt.% MgO lie on trends of low TiO_2 and FeO^T (Figure 2) that most likely reflect fractional crystallization and thus imply that these lavas are evolved melts from boninitic parental magmas (Pearce & Reagan, 2019). Thus, we combine them with the DR boninites as one group, following the reasoning of Crawford et al. (1989) and Pearce and Reagan (2019). Lavas from Tafahi and Niuatoputapu in the Tofua island arc also have low TiO_2 but higher FeO^T contents (Figure 2) and their resemblance to boninites has been suggested previously (e.g., Cooper et al., 2010). The variation of Si8.0 and Ti8.0 support the fact that distinct magmas with relatively low Ti8.0 and high Si8.0 erupt on the Tonga Microplate (DR, Mata volcanoes, Tafahi) and along the FSC, all of which either fall into the field of boninite or

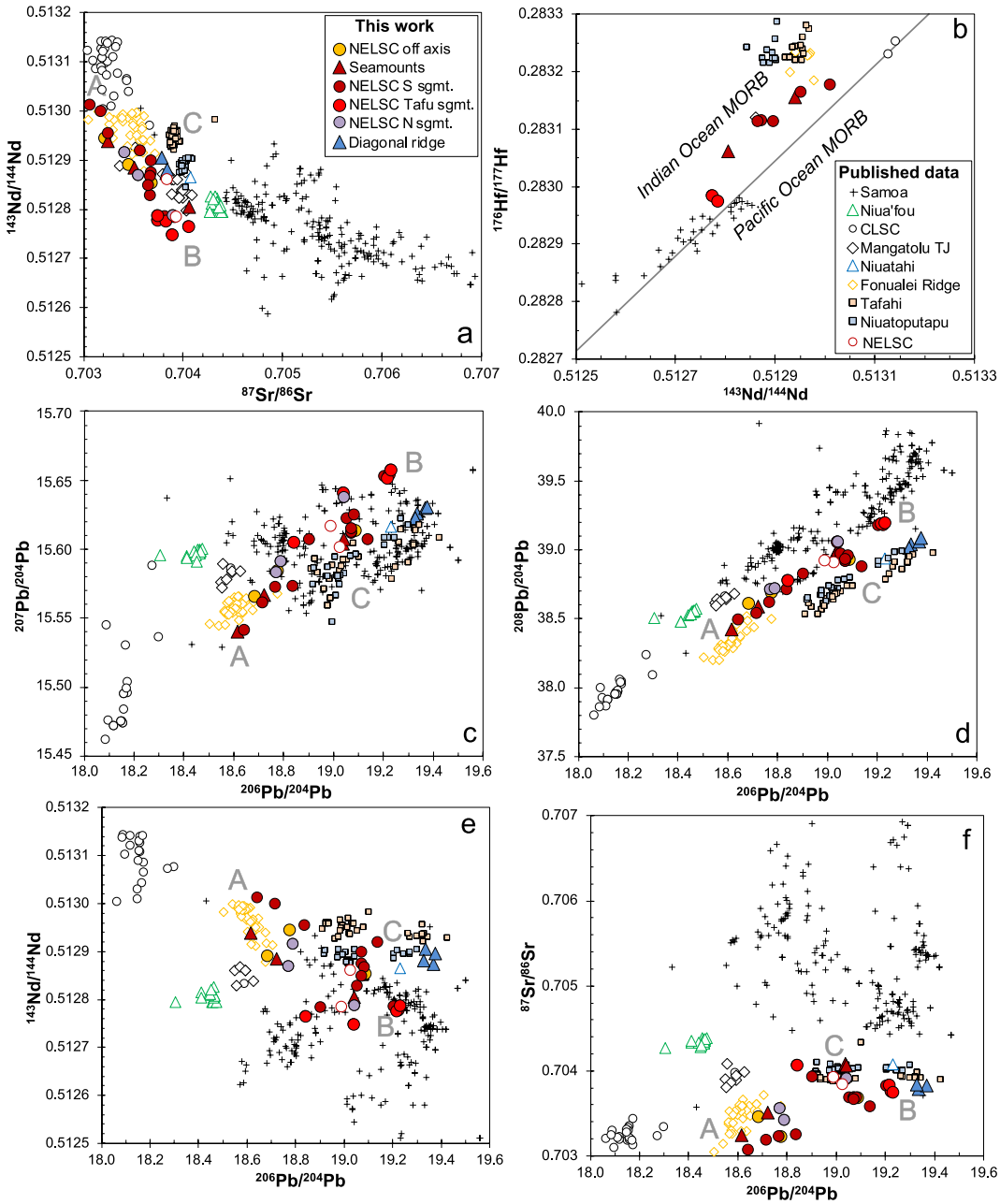

Figure 7. Isotopic variations of Northeast Lau Spreading Center and diagonal ridge samples showing (a) $^{143}Nd/^{144}Nd$ versus $^{87}Sr/^{86}Sr$, (b) $^{176}Hf/^{177}Hf$ versus $^{143}Nd/^{144}Nd$, (c) $^{207}Pb/^{204}Pb$ versus $^{206}Pb/^{204}Pb$, (d) $^{208}Pb/^{204}Pb$ versus $^{206}Pb/^{204}Pb$, (e) $^{143}Nd/^{144}Nd$ versus $^{206}Pb/^{204}Pb$, and (f) $^{87}Sr/^{86}Sr$ versus $^{206}Pb/^{204}Pb$, in comparison to Magatolu Triple Junction, Fonualei Spreading Center, and Niuatahi Volcano rocks as well as Samoa hotspot basalts. Data sources as in Figure 2, and Samoa basalts as in Figure 5. The division line between Indian Ocean and Pacific Ocean-type MORB is from Pearce et al. (2007).

have a boninite resemblance (Figure 3a). Importantly, the lavas with the lowest Ti8.0 also have the highest H_2O/Ce ratios (>0.6, Figure 3b) implying relatively high water contents in the depleted mantle. Typically, boninitic lavas are believed to form by fluid-induced melting of a highly depleted mantle with little or no clinopyroxene (Crawford et al., 1989; Parman & Grove, 2004; Pearce & Reagan, 2019), which implies a residual harzburgitic mantle beneath the northern Tonga Microplate. Interestingly, this harzburgitic mantle source occurs immediately east of the NELSC beneath the Tonga Microplate, that is, some 10 km off-axis (Figure 1). Thus, highly depleted but water-rich mantle occurs east of the NELSC beneath the Tonga Microplate (Figure 1) and the DR

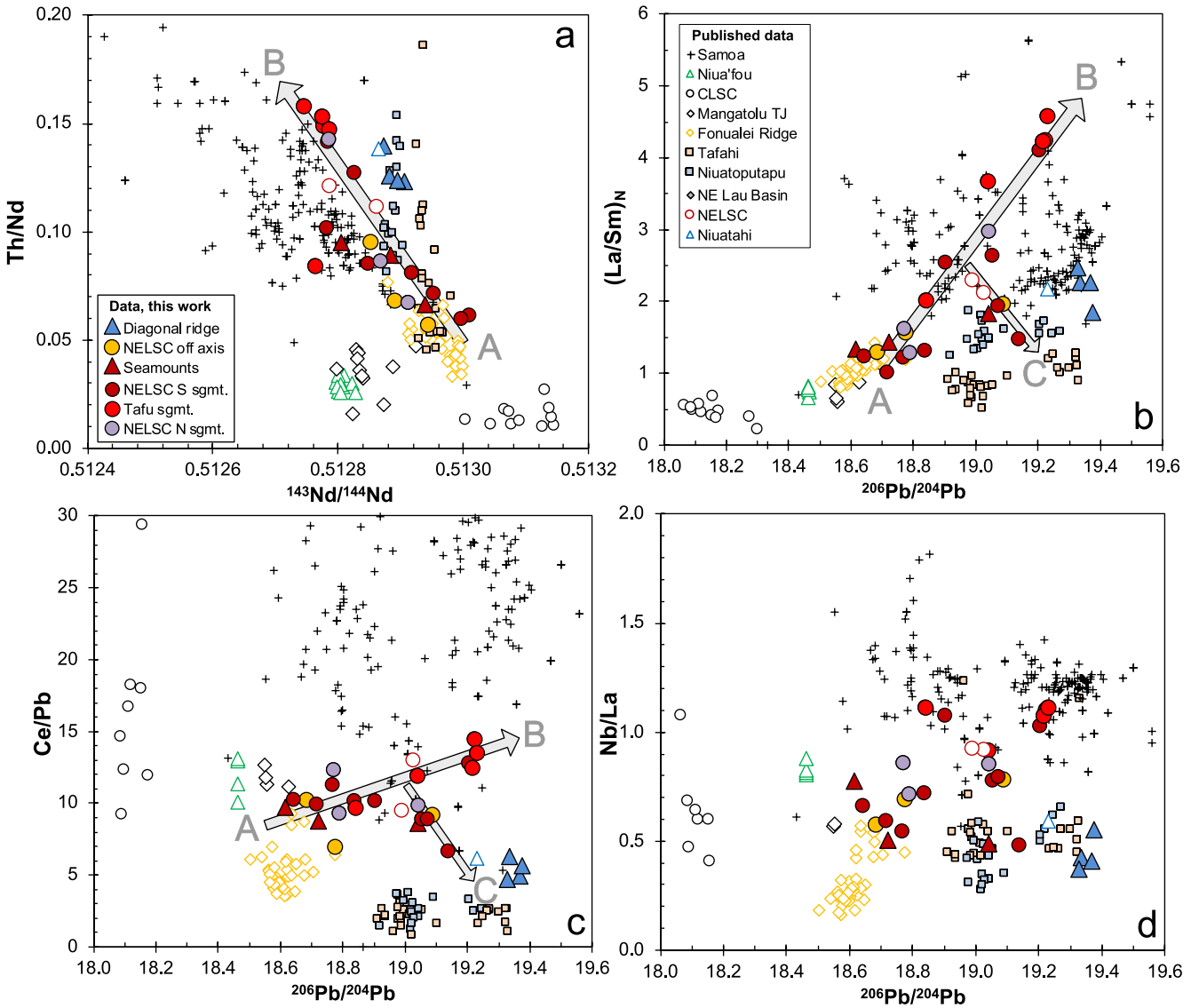

Figure 8. Selected incompatible element ratios (a) Th/Nd versus $^{143}Nd/^{144}Nd$, (b) $(La/Sm)_N$ versus $^{206}Pb/^{204}Pb$, (c) Ce/Pb versus $^{206}Pb/^{204}Pb$, and (d) Nb/La versus $^{206}Pb/^{204}Pb$ for the Northeast Lau Spreading Center and DR lavas in comparison to Magatolu Triple Junction, Fonualei Spreading Center, and Niuatahi Volcano rocks as well as Samoa hotspot basalts. Data sources as in Figure 2, and Samoa basalts as in Figure 6. The arrows show the mixing relations between the three end-members A, B, and C, whose estimated locations are also shown.

and Niuatahi lavas show low Na_2O contents at a given MgO similar to the FSC and Mata lavas (Figure 2d) implying high total degrees of melting of a very depleted mantle.

Previously, Escrig et al. (2012) studied the FSC lavas and suggested that a boundary between the less depleted mantle in the north and highly depleted mantle in the south is situated directly south of the MTJ (Figure 1), and that the FSC boninite signature reflects extremely high degrees of partial melting of up to 38%. Caulfield et al. (2012) proposed that the MTJ magmas formed by decompression melting whereas those of the FSC were generated by fluid-fluxed melting. The distinct composition of the tholeiitic NELSC lavas from the boninitic DR and Niuatahi lavas implies (a) a relatively sharp mantle boundary and (b) that the melting zones and magma ascent systems of the NELSC and the neighboring DR and Niuatahi are largely separate, even though they lie very close. Whereas fertile mantle flows into the NELSC melting region, the mantle further east beneath the northern Tonga Microplate has been depleted to harzburgite by previous melting (Falloon & Danyushevsky, 2000). Such a sharp change of magma compositions and crustal structure is also observed further to the south at the Eastern Lau Spreading Center and has been explained with the change in viscosity between the hydrated and dry portion

of the mantle wedge (Dunn & Martinez, 2011; Sleeper & Martinez, 2014). We suggest that a similar boundary between hydrated ($H_2O/Ce > 0.6$, Figure 3b) and dry mantle ($H_2O/Ce < 0.6$, Figure 3b) exists east of the NELSC (Figure 1) where the DR and Niuatahi volcanoes formed from magmas ascending in the low-viscosity hydrated mantle indicated by relatively high Ba/Nb > 35 and low Ce/Pb < 7 in the lavas (Figure 6). This boundary probably also separates a western decompression melting zone from a zone of fluid-fluxed melting in the east, similar to models for other back-arc basin spreading axes suggested by Langmuir et al. (2006). The highly depleted harzburgitic composition of this hydrated portion of the mantle is in agreement with geophysical models (Sleeper & Martinez, 2014) predicting decoupling of this mantle from the dry fertile mantle distant from the island arc. The depletion implies restricted convection of the hydrous mantle with repeated melting of the peridotite.

5.2. Mixing Processes and Definition of the Mantle End-Members

The trends of the radiogenic isotope and incompatible element ratios of the NELSC and seamount lavas (Figures 6 and 7) suggest mixing of different magma sources. Because all of these lavas are basaltic to andesitic the mixing probably occurs in the mantle rather than in the shallow crust. Assimilation of sediments or hydrothermally altered basaltic rocks is known to affect ascending magmas in oceanic lithosphere (Michael & Cornell, 1998; Wanless et al., 2011), but it is unlikely that the young crust of the NELSC contains significant sediments. Assimilation of hydrothermally altered upper crustal rocks in MORB is typically reflected by variable Cl/K (Michael & Cornell, 1998), but the relatively constant Cl/K ratios in the NELSC lavas between 7.9 and 3.8 wt.% MgO (Figure 2f) do not indicate assimilation. Rather, the high Cl/K in NELSC and DR glasses are due to subduction of Cl, although we do not find a correlation between Cl/K and tracers for slab input like Ce/Pb or U/Nb (not shown). The correlation of incompatible element and isotope ratios like, for example, Th/Nd and $(La/Sm)_N$ with $^{143}Nd/^{144}Nd$ and $^{206}Pb/^{204}Pb$, respectively (Figure 8), implies that the sources have distinct isotope and incompatible element compositions. Thus, two of the sources are relatively depleted in incompatible elements with low $(La/Sm)_N$ and Th/Nd, whereas another source is enriched (Figure 8). The radiogenic isotope and incompatible element ratios (Figures 6–8) indicate three mixing end-members affecting magmas along the NELSC axis: End-member A occurs in some NELSC and southern seamount lavas and has relatively high $^{143}Nd/^{144}Nd$ ratios of ~0.51295, but low $^{87}Sr/^{86}Sr \sim 0.7032$ and Pb isotope ratios of $^{206}Pb/^{204}Pb \sim 18.65$. End-member A is relatively depleted in incompatible elements similar to the source of lavas from the northern FSC and has $(La/Sm)_N \sim 1$ and Ce/Pb of 10 (Figure 5). End-member B has radiogenic Pb isotope ratios ($^{206}Pb/^{204}Pb > 19.2$), but low $^{143}Nd/^{144}Nd \sim 0.5127$ and $^{87}Sr/^{86}Sr \sim 0.704$, and high $(La/Sm)_N$ and Nb/Zr. This component is most clearly observed in some incompatible element enriched basalts from the central NELSC. Similar isotopic compositions with high $^{206}Pb/^{204}Pb$ but relatively low $^{87}Sr/^{86}Sr$ were also found in boninites that were dredged west of the northernmost NELSC rift tip (Falloon et al., 2007). The incompatible element-depleted end-member C with high Pb and intermediate Sr and Nd isotope ratios is evident in the boninitic lavas from Niuatahi and DR (Falloon et al., 2007), but also affects some of the NELSC lavas (Figure 8). The variations in Pb isotopes and Ce/Pb with $^{206}Pb/^{204}Pb$ indicate that most NELSC basalts represent mixtures between end-members A and B. A mixture of these two components with $^{206}Pb/^{204}Pb \sim 19.0$ is mixing with end-member C yielding some of the NELSC magmas, particularly those close to the Tafu segment (Figures 5 and 8c). The trends observed, for example, in $^{208}Pb/^{204}Pb$ versus $^{206}Pb/^{204}Pb$ (Figure 7) and in Ce/Pb versus $^{206}Pb/^{204}Pb$ (Figure 7c) imply that end-member C affects the mantle or the magmas after mixing of the components A and B. Most likely, a small portion of partial melt from end-member C flows from the melting region of Niuatahi and the DR into the axial melting region beneath the NELSC. However, this mixing has no significant effect on the major element composition of the NELSC magmas as discussed above.

5.3. End-Member A: The Relatively Depleted Mantle Source

The isotope composition of incompatible element-depleted end-member A (e.g., $^{143}Nd/^{144}Nd \sim 0.51295$, $^{206}Pb/^{204}Pb \sim 18.65$) is observed in lavas between 15.3° and 16.5°S from the southern NELSC, the southern seamounts, and the northernmost basalts from the FSC (Figures 4 and 7). The FSC lavas show gradients in incompatible element with less depleted lavas in the north, and Nd and $^{206}Pb/^{204}Pb$ isotope ratios that overlap with those of the NELSC, where the northernmost samples from the FSC resemble the southern seamount lavas from the NELSC (Figure 4). Consequently, end-member A appears to occur mainly in the north beneath the southern NELSC and northern FSC, whereas the southern FSC erupts more incompatible element-depleted lavas, for example, with

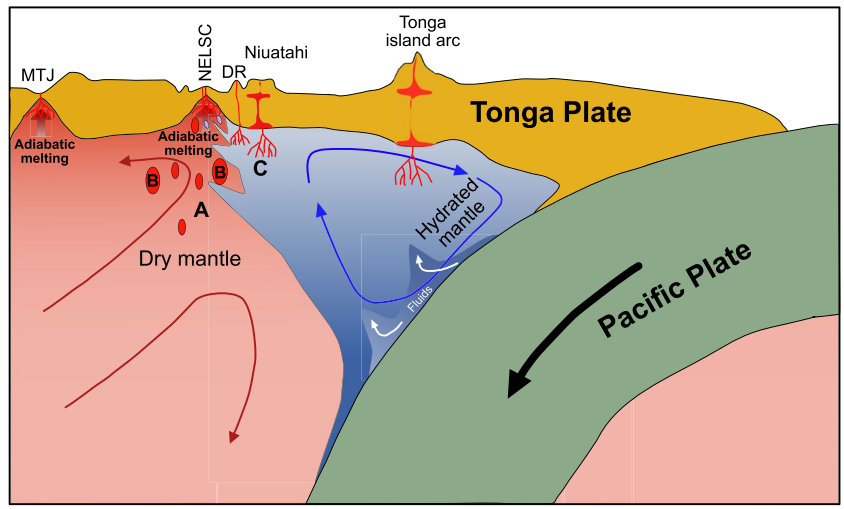

Figure 9. Cartoon of the different mantle portions beneath the Tonga and the Niua'fou Plates redrawn after Sleeper and Martinez (2014). The sharp geochemical boundary between the off-axis diagonal ridge and Niuatahi lavas in the east and the Northeast Lau Spreading Center lavas in the west may reflect the boundary between dry and hydrated mantle and the viscosity contrast between these. The dry mantle part consists of a depleted peridotite matrix of end-member A with some enriched portions of of end-member B. Convection in the low-viscosity hydrated mantle wedge may cause increased depletion of the mantle and the storage and transport of old slab components like those from the Louisville Seamount Chain (end-member C) into the rear-arc magmas. The boundary also marks the change from adiabatic decompression melting in the west from fluid-fluxed melting in the east.

Nb/La < 0.4 (Figures 5 and 6). The distinct composition of the NELSC lavas compared to those from the MTJ some 40 km to the west indicates that there is no eastward-directed flow of the mantle, that is, no corner flow in agreement with shear-wave splitting results (Smith et al., 2001). The Hf and Nd isotope composition of the relatively depleted NELSC lavas indicates that this mantle resembles the Indian Ocean MORB domain as defined previously for the SW Pacific Ocean (Pearce et al., 2007). Although there is a general gradient in many incompatible element and Nd and Pb isotope ratios (Figure 5), the variation at any location along the NELSC and FSC indicates a small-scale heterogeneity of the mantle and mixing between end-member A and the more enriched end-member B. We suggest that this implies a variable abundance of the two components in the upper mantle beneath the NELSC. In contrast to the end-member C of the boninitic lavas of DR and Niuatahi, end-member A mantle is fertile with relatively high TiO_2 contents and yields tholeiitic basaltic melts typical for <20% partial melting of lherzolitic mantle (Kushiro, 2007).

The ratios of Th/Nd < 0.06, Cl/K ~ 0.25, and Ba/Nb ~ 20 (Figures 2, 5, and 6) in NELSC basalts are generally slightly higher than those of average MORB with Th/Nd of 0.02, Cl/K < 0.08, and Ba/Nb < 10 (Hofmann, 1988; Michael & Cornell, 1998), indicating that end-member A has previously been influenced by a slab component enriched in fluid-mobile elements like Th, Cl, and Ba. The slab influence is also reflected by relatively high contents of large ion lithophile elements (LILE, e.g., Rb, K, Sr), and a negative Nb-Ta trough in the MORB-normalized incompatible element patterns (Figure 4). This slab component is most clearly seen in the lavas from seamounts at the southern NELSC tip because they show the highest U/Nb and Ba/Nb (Figure 6). We conclude that the entire mantle beneath the NELSC and FSC is affected by a slab component, but the effect increases toward the south causing increasing Ba/Nb and decreasing Ce/Pb (Figure 5) because the FSC is closer to the island arc than the NELSC. The slab component most likely consists of a hydrous fluid fractionating Cl from K and Pb from Ce (Figure 6). Thus, although a sharp boundary appears to occur between the melting zones and mantle sources beneath the NELSC and the neighboring DR, there is some transport of fluid-mobile elements into the melting zone of the NELSC (Figure 9).

5.4. Origin of the Enriched Mantle End-Member B With Radiogenic Pb Isotopes

End-member B has low $^{143}Nd/^{144}Nd$ of ~ 0.51275, intermediate $^{87}Sr/^{86}Sr$ of 0.704, and Pb isotope ratios with $^{206}Pb/^{204}Pb$ of >19.2 (Figure 7), and is most clearly identified in basalts from Tafu segment at 15.37°S

(Figure 5). Similar isotope compositions were also found in boninitic lavas (e.g., samples 16-9/1 and 16-10/4) that were recovered some 20 km west of the NELSC at the Vitiaz Fracture Zone (Falloon et al., 2007). This end-member is incompatible element-enriched, producing melts with $(La/Sm)_N > 4$, Nb/La > 1, and relatively high Ce/Pb ~ 14, but low Ba/Nb ~ 10 (Figures 6 and 8) compared to island arc lavas, reflecting an enriched mantle source resembling that of oceanic island basalts (OIB). The Tafu lavas have similar TiO_2, FeO^T, and Na_2O at 8 to 7 wt.% MgO to the other NELSC basalts (Figure 2) indicating that lower degrees of partial melting cannot be the cause for the stronger enrichment of incompatible elements. The Ce/Pb of these enriched NELSC samples are lower than the ratio of 25 typically found in OIB (Hofmann et al., 1986), which could indicate a slab component affecting the entire mantle beneath the NELSC (Figure 5e). In this case, there appears to be a smaller effect on the enriched end-member B than on the more depleted mantle end-member A which has lower Ce/Pb (Figure 6d). Alternatively, the low Ce/Pb reflects an OIB-type source like the Samoan plume where some basalts also have Ce/Pb as low as 10 (Figure 6d). The Cl/K of 0.2–0.3 in the enriched NELSC lavas, for example, from Tafu segment (Figure 2f) could indicate a slab component, but some OIB also have high Cl/K due to recycling of seawater (e.g., Stroncik & Haase, 2004). Because the basalts reflecting enriched end-member B also have low Ba/Nb similar to some Samoan lavas, but unlike the slab-affected lavas from the FSC and arc front (Figure 6b) we conclude that end-member B is indeed OIB-type mantle. This OIB-type source resides as heterogeneities in the upper mantle beneath the NELSC and is apparently most abundant beneath the Tafu segment between 15.2 and 15.5°S (Figure 5). The fact that end-member B is not a slab component rules out an origin from subducted material of the Cook-Austral volcanic chains that appear to affect volcanoes further to the west of the NELSC (Price et al., 2016).

The incompatible element-enriched NELSC lavas and particularly the decreasing gradients in $^{206}Pb/^{204}Pb$ and Nb/La (Figure 5) may indicate a southward-directed influx of Samoan plume mantle that has previously been proposed for the northern Lau and Tonga region (e.g., Danyushevsky et al., 1995; Ewart et al., 1998; Poreda & Craig, 1992; S. Turner & Hawkesworth, 1998; Wendt et al., 1997). The Samoa lavas typically have high $(La/Sm)_N$, Ce/Pb of >10, and Nb/La > 1, and thus the northwards-directed increasing trends of these ratios along the NELSC (Figure 5) could indicate an inflow of Samoa plume material. However, the NELSC lavas with the highest $^{206}Pb/^{204}Pb$ have lower $^{208}Pb/^{204}Pb$ and $^{87}Sr/^{86}Sr$ but higher $^{207}Pb/^{204}Pb$ than Samoa OIB (Figure 7). Thus, the known Samoan lavas do not represent the incompatible element-enriched mantle component affecting the NELSC lavas and we suggest that the NELSC magmas form from a different source. Our results agree with previous studies finding MORB-like He isotope compositions of 8.0–8.4 R/Ra in NELSC lavas, that do not show evidence of Samoan plume material unlike volcanic rocks of the NW Lau Basin (Lupton et al., 2009, 2015). Alternatively, the OIB-like component B may be included in southwards flowing mantle from the "South Pacific Isotopic and Thermal Anomaly" (SOPITA) as suggested by Pearce et al. (2007) or from a HIMU-type OIB source like it is observed in the Cook-Austral hotspot (Falloon et al., 2007). However, there is no active mantle plume directly north of the NELSC and the volcanoes of the Cook-Austral chains in this region have ages of 20–30 Ma (Price et al., 2016), that is, they cannot be the source of plume mantle. End-member B does not show the high Ce/Pb of ~30 or the radiogenic Pb isotope compositions (e.g., $^{206}Pb/^{204}Pb > 20$) typical for HIMU-type OIB (e.g., Hanyu et al., 2013; Sun & McDonough, 1989). The MORB-like He isotope ratios of NELSC lavas (Lupton et al., 2015) indicate that the incompatible element-enriched end-member B probably resides in the upper mantle and has not experienced a contribution of a primordial, deep mantle source. Thus, we do not find evidence for a contribution by a deep mantle plume source to the NELSC magmas. Rather, the incompatible element-enriched component B is largely restricted to the Tafu volcano of the NELSC (Figure 5) and may thus be caused by small-scale enriched mantle heterogeneities underneath the NELSC that have been proposed to exist in the upper mantle (Zindler et al., 1984). Such enriched heterogeneities may also produce more magma because the mantle is more fertile and causes seamount formation both along spreading axes and back-arc rifts (Davis & Karsten, 1986; Lima et al., 2017). We suggest that the enriched end-member B probably represents heterogeneities in the upper mantle that are tapped to variable extent by melting along the NELSC, but an inflow of compositionally variable plume material from the SOPITA region cannot be excluded.

5.5. The Origin of End-Member C Observed in Diagonal Ridge Lavas

End-member C is observed in the boninitic DR lavas and has isotopic compositions closely resembling the rocks from Tafahi and Niuatoputapu islands in the northern Tofua island arc (Figure 7). Additionally, several NELSC lavas show trends in Pb isotopes toward the DR samples (Figure 6d) which is also observed in $(La/Sm)_N$

and Ce/Pb versus $^{206}Pb/^{204}Pb$ (Figure 8). The DR samples are also similar to Tafahi and Niuatoputapu lavas in terms of low Ce/Pb and Nb/La, although they have slightly higher $(La/Sm)_N$ (Figure 8). Thus, similarly to the mantle wedge beneath Tafahi and Niuatoputapu (Beier et al., 2017; Ewart et al., 1998; S. Turner et al., 1997), the mantle beneath the DR and Niuatahi volcano was affected by subduction of material from the LSC (Figure 7). The Pb isotope signatures of the DR lie on a narrow range comparable to, but slightly more radiogenic than that from Niuatahi volcano (Figure 7). We propose that the recycled LSC component is not geographically restricted to Niuatoputapu and Tafahi, but also occurs further west in the Lau Basin, in agreement with previous results (Falloon et al., 2007). Both $^{207}Pb/^{204}Pb$ and $^{208}Pb/^{204}Pb$ of DR and Niuatahi are lower at a given $^{206}Pb/^{204}Pb$ than the NELSC samples (Figures 7d and 7e). Thus, as pointed out above, the incompatible elements and radiogenic isotope ratios in some NELSC magmas indicate addition of DR melts following mixing of end-members A and B (Figures 7 and 8). The high SiO_2 and low TiO_2 contents of the DR lavas resemble boninites that are also known from Niuatahi and the Mata volcanoes further to the east (Figure 2), but distinct from the NELSC lavas. Thus, we suggest that the melting zones of the NELSC and DR/Niuatahi are distinct with a sharp boundary between relatively fertile mantle beneath the NELSC and depleted harzburgite in the eastern off-axis region. Only highly incompatible elements and radiogenic isotopes are affected by flow of material, probably in the form of small degree partial melts from the off-axis region into the NELSC axis. The low Ce/Pb and Nb/La but high Th/Nd of end-member C indicates a component from the subducted slab, and thus the depleted harzburgite mantle most likely is hydrated, which is supported by the relatively high H_2O/Ce ratios of two studied DR lavas (Figure 3b). We agree with Falloon et al. (2007) that similar to the arc front at Tafahi, the LSC component beneath the Tonga Microplate is mixed into the harzburgitic mantle beneath the DR and Niuatahi causing partial melting. Hydrated mantle peridotite has a viscosity at least one order of magnitude lower than dry peridotite (Billen & Gurnis, 2001; Hirth & Kohlstedt, 2003), which can explain the sharp boundary between the NELSC back-arc axis and the Tonga Microplate rear-arc volcanism. Because of the low viscosity of this hydrated mantle wedge portion, convection may cause repeated partial melting leading to extreme depletion of the mantle, but may also transport slab components into the rear-arc melting zone several millions of years after the LSC was subducted (Ruellan et al., 2003).

5.6. Along-Axis Variation of the Composition of NELSC, MTJ, and FSC Lavas

Unfortunately, only few data exist on the NELSC north of 15.2°S, but lavas between 15.2° and 18°S generally show increasing Ba/Nb and decreasing in Ce/Pb, Nb/La, and $^{206}Pb/^{204}Pb$ from north to south. However, the change is mainly due to the compositional trend of the FSC lavas, whereas the chemical and isotopic variation of basalts erupting along the NELSC is much larger on a small scale and not systematic (Figure 4). On the one hand, this could imply a shallow inflow of heterogeneous mantle containing variable amounts of end-members A and B from the north around the subducting slab. On the other hand, the most enriched lavas with the highest $(La/Sm)_N$, Nb/La, and $^{206}Pb/^{204}Pb$ occur at Tafu segment at 15.3°S, that is, there is no clear gradient from the north. Thus, the presence of the most enriched material beneath Tafu segment may indicate that the mantle enriched in end-member B is ascending vertically beneath the axis rather than flowing in laterally. Phase velocity anisotropy in the mantle beneath the northern Lau Basin is approximately parallel to the spreading axis which was interpreted to reflect inflow of Samoan plume mantle, but seismic velocities at 100 km depth beneath the NELSC are relatively high, implying relatively cold mantle (Wei et al., 2016). Consequently, there is no geochemical and geophysical evidence for inflow of hot mantle from the Samoan plume, but more high-resolution seismic studies are required to rule out an inflow shallower than 100 km. The fact that MTJ lavas further west have higher Ce/Pb and lower Ba/Nb (Figure 5) than the NELSC lavas at the same latitude suggests a MORB-like mantle beneath the MTJ compared to the OIB-type mantle beneath the NELSC.

On a larger scale, the radiogenic isotopes show that no simple mixing relations exist between the NELSC, MTJ, and FSC sources (Figure 7). Whereas the NELSC and northern FSC lavas show some overlap, implying that they share end-member A, the volcanic rocks from the MTJ have very different compositions and isotope trends. This confirms the presence of different mantle sources beneath the NE and NW Lau Basin. The similarity of incompatible element as well as Nd and Pb isotope ratios of the northern FSC and southern NELSC lavas (Figures 5 and 8) suggests that the back-arc region between 15.4° and 16.3°S has the same mantle source affected by approximately the same slab component. The low $(La/Sm)_N$ and Nb/La indicate that this mantle is relatively depleted in incompatible elements compared to the mantle further north. This is the region where the back-arc axis is most distant to the arc and where rifting is absent between 16.0° and 15.7°S, although small volcanoes occur in

this region (Figure 1). Further to the south the FSC lies closer to the arc front than the NELSC, and it has been suggested that the back-arc melting region captured that of the arc front, because there appears to be no active volcanism in the arc front (Escrig et al., 2012; Keller et al., 2008). In contrast, the two young large volcanic structures of Tafahi and Niuatoputapu lie in the arc front east of the gap in the back-arc rifts (Figure 1a). Thus, in this region most of the magma is erupted in the arc front and only little at single, isolated small volcanoes in the back-arc. The variable distribution of the slab component and hydrated mantle may thus affect the formation of back-arc rifts and spreading axes. The young NELSC rift axis may have formed at the boundary between hydrated and dry peridotite due to the viscosity contrast in the mantle wedge that caused variable mantle behavior during rollback of the Pacific Plate.

5.7. Evidence for a Narrow Melting Zone Beneath the Southward-Propagating NELSC

Lavas erupted between the northern tip of the MTJ and Niuatahi volcano show highly variable geochemical compositions over a distance of about 80 km (Figure 5). Whereas the Tafu segment samples are very enriched in incompatible elements, the northern and southern NELSC segments show much less enrichment and high $^{143}Nd/^{144}Nd$ (Figures 5a and 5b). As discussed above, the isotope compositions indicate that the MTJ source does not affect the NELSC magmas, implying no eastward-directed mantle flow in this region. Additionally, although the Tafu segment on the NELSC lies only 15 km distant to the DR (Figure 1b), there is very limited mixing between the magmas or sources. Spreading axes and particularly those with high spreading rates >50 mm/year typically have wide melting regions of 200 km width (Key et al., 2013; The MELT Seismic Team, 1998). The spreading rate at the NELSC is estimated at 42 mm/year (Baxter et al., 2020), but the highly variable composition of the NELSC lavas and their distinct composition to the off-axis volcanic rocks implies a narrow melting zone similar to those suggested in continental rift areas (Schmeling, 2010). In these models a wide melting zone forms only after 3 million years of rifting (Schmeling, 2010), which implies an age <3 Ma for the NELSC. Such a young age is in agreement with the narrow rift basin of ~20 km width of the Tafu segment and with the southward propagation of the NELSC (Figure 1). We conclude that the volcanic ridges forming the NELSC each represent separate magmatic systems that are fed by ascending dykes. The large compositional variation implies separate magma batches rising in a narrow melting region without mixing with melts from neighboring volcanic structures. Such distinct magma ascent pathways in the melting region beneath the NELSC support the concept of melt channels in the upper mantle (Kelemen et al., 1997; Wanless & Behn, 2017).

6. Conclusions

Figure 9 shows the model we suggest to explain the variation of the compositions of the lavas in the NE Lau Basin. The NELSC propagates southwestwards into older crust, causing formation of numerous seamounts at the propagator similar to the northward propagating FSC. The young volcanic structures of the DR and Niuatahi lie on the eastern flank of the NELSC, but there is only limited mixing of DR components into NELSC melts (Figure 9). Fluid-mobile elements are most enriched in the DR and Niuatahi lavas whereas the neighboring NELSC lavas are less affected by the slab. The sharp geochemical boundary between harzburgitic mantle beneath the Tonga Microplate in the east and the fertile mantle of the propagating NELSC probably reflects the boundary between hydrous and dry mantle (Figure 9). The hydrous mantle with low viscosity has been repeatedly depleted by partial melting but provides more magma due to input of hydrous slab components. Three isotopic end-members are defined where the depleted end-member A of the southern NELSC lavas resembles that of the northernmost lavas of the FSC and forms the matrix of the dry mantle (Figure 9). This end-member represents Indian Ocean-type upper mantle and contains variable amounts of enriched component B (Figure 9) that is most clearly defined by Tafu segment lavas. End-member B is distinct from known Samoa or HIMU-type hotspot lavas and thus is apparently not related to southward-directed influx of Samoan plume mantle or SOPITA mantle in general. The propagating rift tip of the southern NELSC is volcanically active with several small seamounts and these resemble the NELSC lavas further north in forming from a relatively incompatible element-depleted mantle. This relatively incompatible element-depleted but otherwise fertile mantle end-member A provides the magmas of the propagating rift largely by adiabatic decompression melting because there is little influx of a slab component (Figure 9). In contrast, the DR lavas show the influence of a component from the subducted LSC similar to the arc volcanoes Niuatoputapu and Tafahi (end-member C) which reflects the transport of old slab components into the rear-arc, that are possibly trapped in the low-viscosity mantle wedge portion. The addition of

water causes fluid-fluxed melting in this depleted portion of the mantle (Figure 9). The highly variable composition of NELSC lavas on a small scale indicates distinct magma ascent in dikes and a narrow melting zone beneath the rift with little interaction with off-axis magmas or mantle sources. Our results show the complexity of back-arc magma formation with the effects of the slab component on numerous mantle sources, the variable mixing and melting processes and their dependence on the mantle composition, and the possible consequences of the mantle on tectonic processes such as lithospheric rifting.

Data Availability Statement

All data used in this manuscript are found in Table S1 and geochemical data is available in the PANGAEA data repository https://doi.org/10.1594/PANGAEA.941306.

Acknowledgments
The authors thank Captain O. Meyer and his crew for the help and effort during SO263 Tonga Rift. The authors gratefully acknowledge the professional help and support of V. Ratmeyer and the team of ROV MARUM Quest. The authors thank T. Ireland at ANU for his help and support during the water analysis. Careful and constructive reviews by L. Danyushevsky, M. Jackson, and an anonymous reviewer helped to improve the quality of this work. This work was funded by project BE4459/8-1 from the Deutsche Forschungsgemeinschaft (DFG), and project 03G0263A of the Bundesministerium für Bildung und Forschung (BMBF). Open access funding enabled and organized by Projekt DEAL.

References

Baker, E. T., Lupton, J. E., Resing, J. A., Baumberger, T., Lilley, M. D., Walker, S. L., & Rubin, K. H. (2011). Unique event plumes from a 2008 eruption on the Northeast Lau Spreading Center. *Geochemistry, Geophysics, Geosystems*, *12*(9), Q0AF02. https://doi.org/10.1029/2011GC003725

Baker, E. T., Walker, S. L., Massoth, G. J., & Resing, J. A. (2019). The NE Lau Basin: Widespread and abundant hydrothermal venting in the back-arc region behind a superfast subduction zone. *Frontiers in Marine Science*, *6*, 382. https://doi.org/10.3389/fmars.2019.00382

Baxter, A. T., Hannington, M. D., Stewart, M. L., Emberley, J. M., Breker, K., Krätschell, A., et al. (2020). Shallow seismicity and the classification of structures in the Lau back-arc basin. *Geochemistry, Geophysics, Geosystems*, *21*(7), e2020GC008924. https://doi.org/10.1029/2020GC008924

Beier, C., Brandl, P. A., Lima, S. L., & Haase, K. M. (2018). Tectonic control on the genesis of magmas in the New Hebrides arc (Vanuatu). *Lithos*, *312–313*, 290–307. https://doi.org/10.1016/j.lithos.2018.05.011

Beier, C., Turner, S. P., Haase, K. M., Pearce, J. A., Münker, C., & Regelous, M. (2017). Trace element and isotope geochemistry of the northern and central Tongan islands with an emphasis on the genesis of high Nb/Ta signatures at the northern volcanoes of Tafahi and Niuatoputapu. *Journal of Petrology*, *58*(6), 1073–1106. https://doi.org/10.1093/petrology/egx047

Bevis, M., Taylor, F. W., Schutz, B. E., Recy, J., Isacks, B. L., Helu, S., et al. (1995). Geodetic observations of very rapid convergence and back-arc extension at the Tonga arc. *Nature*, *374*(6519), 249–251. https://doi.org/10.1038/374249a0

Billen, M. I., & Gurnis, M. (2001). A low viscosity wedge in subduction zones. *Earth and Planetary Science Letters*, *193*(1–2), 227–236. https://doi.org/10.1016/S0012-821X(01)00482-4

Bonnardot, M.-A., Régnier, M., Ruellan, E., Christova, C., & Tric, E. (2007). Seismicity and state of stress within the overriding plate of the Tonga-Kermadec subduction zone. *Tectonics*, *26*(5), TC5017. https://doi.org/10.1029/2006TC002044

Brandl, P. A., Beier, C., Regelous, M., Abouchami, W., Haase, K. M., Garbe-Schönberg, D., & Galer, S. J. G. (2012). Volcanism on the flanks of the East Pacific Rise: Quantitative constraints on mantle heterogeneity and melting processes. *Chemical Geology*, *298–299*, 41–56. https://doi.org/10.1016/j.chemgeo.2011.12.015

Caulfield, J., Turner, S. P., Arculus, R. J., Dale, C., Jenner, F. E., Pearce, J. A., et al. (2012). Mantle flow, volatiles, slab-surface temperatures and melting dynamics in the north Tonga arc–Lau back-arc basin. *Journal of Geophysical Research*, *117*(B11), B11209. https://doi.org/10.1029/2012JB009526

Chauvel, C., Bureau, S., & Poggi, C. (2011). Comprehensive chemical and isotopic analyses of basalt and sediment reference materials. *Geostandards and Geoanalytical Research*, *35*(1), 125–143. https://doi.org/10.1111/j.1751-908X.2010.00086.x

Compston, W., & Oversby, V. M. (1969). Lead isotopic analysis using a double spike. *Journal of Geophysical Research*, *74*(17), 4338–4348. https://doi.org/10.1029/JB074i017p04338

Cooper, L. M., Plank, T., Arculus, R. J., Hauri, E. H., Hall, P. S., & Parman, S. W. (2010). High-Ca boninites from the active Tonga Arc. *Journal of Geophysical Research*, *115*(B10), B10206. https://doi.org/10.1029/2009JB006367

Crawford, A. J., Falloon, T. J., & Green, D. H. (1989). Classification, petrogenesis and tectonic setting of boninites. In A. J. Crawford (Ed.), *Boninites and related rocks* (pp. 1–49). Springer.

Danyushevsky, L. V., Falloon, T. J., Sobolev, A. V., Crawford, A. J., Carroll, M., & Price, R. C. (1993). The H_2O content of basalt glasses from southwest Pacific back-arc basins. *Earth and Planetary Science Letters*, *117*(3–4), 347–362. https://doi.org/10.1016/0012-821X(93)90089-R

Danyushevsky, L. V., Sobolev, A. V., & Falloon, T. J. (1995). North Tongan high-Ca boninite petrogenesis: The role of Samoan plume and subduction zone-transform fault transition. *Journal of Geodynamics*, *20*(3), 219–241. https://doi.org/10.1016/0264-3707(95)00013-Y

Davis, E. E., & Karsten, J. L. (1986). On the cause of the asymmetric distribution of seamounts about the Juan de Fuca Ridge: Ridge-crest migration over a heterogeneous asthenosphere. *Earth and Planetary Science Letters*, *79*(3–4), 385–396. https://doi.org/10.1016/0012-821X(86)90194-9

de Hoog, J. C. M., Koetsier, G. W., Bronto, S., Sriwana, T., & van Bergen, M. J. (2001). Sulfur and chlorine degassing from primitive arc magmas: Temporal changes during the 1982-1983 eruptions of Galunggung (West Java, Indonesia). *Journal of Volcanology and Geothermal Research*, *108*(1–4), 55–83. https://doi.org/10.1016/S0377-0273(00)00278-X

Dunn, R. A., & Martinez, F. (2011). Contrasting crustal production and rapid mantle transitions beneath back-arc ridges. *Nature*, *469*(7329), 198–202. https://doi.org/10.1038/nature09690

Embley, R. W., & Rubin, K. H. (2018). Extensive young silicic volcanism produces large deep submarine lava flows in the NE Lau Basin. *Bulletin of Volcanology*, *80*(4), 36. https://doi.org/10.1007/s00445-018-1211-7

Escrig, S., Bézos, A., Langmuir, C. H., Michael, P. J., & Arculus, R. J. (2012). Characterizing the effect of mantle source, subduction input and melting in the Fonualei Spreading Center, Lau Basin: Constraints on the origin of the boninitic signature of the back-arc lavas. *Geochemistry, Geophysics, Geosystems*, *13*(10). https://doi.org/10.1029/2012GC004130

Ewart, A., Collerson, K. D., Regelous, M., Wendt, J. I., & Niu, Y. (1998). Geochemical evolution within the Tonga-Kermadec-Lau Arc-Back-arc systems: The role of varying mantle wedge composition in space and time. *Journal of Petrology*, *39*(3), 331–368. https://doi.org/10.1093/petroj/39.3.331

Falloon, T. J., & Crawford, A. J. (1991). The petrogenesis of high-calcium boninite lavas dredged from the northern Tonga ridge. *Earth and Planetary Science Letters*, *102*(3–4), 375–394. https://doi.org/10.1016/0012-821X(91)90030-L

Falloon, T. J., & Danyushevsky, L. V. (2000). Melting of refractory mantle at 1.5, 2 and 2.5 GPa under anhydrous and H_2O-saturated conditions: Implications for the petrogenesis of high-Ca boninites and the influence of subduction components on mantle melting. *Journal of Petrology*, *41*, 257–283. https://doi.org/10.1093/petrology/41.2.257

Falloon, T. J., Danyushevsky, L. V., Crawford, T. J., Maas, R., Woodhead, J. D., Eggins, S. M., et al. (2007). Multiple mantle plume components involved in the petrogenesis of subduction-related lavas from the northern termination of the Tonga Arc and northern Lau Basin: Evidence from the geochemistry of arc and backarc submarine volcanics. *Geochemistry, Geophysics, Geosystems*, *8*(9), Q09003. https://doi.org/10.1029/2007GC001619

Fretzdorff, S., Livermore, R. A., Devey, C. W., Leat, P. T., & Stoffers, P. (2002). Petrogenesis of the back-arc East Scotia Ridge, South Atlantic Ocean. *Journal of Petrology*, *43*(8), 1435–1467. https://doi.org/10.1093/petrology/43.8.1435

Freund, S., Haase, K. M., Keith, M., Beier, C., & Garbe-Schönberg, D. (2014). Constraints on the formation of geochemically variable plagiogranite intrusions in the Troodos Ophiolite, Cyprus. *Contributions to Mineralogy and Petrology*, *167*(2), 978. https://doi.org/10.1007/s00410-014-0978-6

Hall, P. S., Cooper, L. B., & Plank, T. (2012). Thermochemical evolution of the sub-arc mantle due to back-arc spreading. *Journal of Geophysical Research*, *117*(B2), B02201. https://doi.org/10.1029/2011JB008507

Hanyu, T., Dosso, L., Ishizuka, O., Tani, K., Hanan, B. B., Adam, C., et al. (2013). Geochemical diversity in submarine HIMU basalts from Austral Islands, French Polynesia. *Contributions to Mineralogy and Petrology*, *166*(5), 1285–1304. https://doi.org/10.1007/s00410-013-0926-x

Harmon, N., & Blackman, D. K. (2010). Effects of plate boundary geometry and kinematics on mantle melting beneath the back-arc spreading centers along the Lau Basin. *Earth and Planetary Science Letters*, *298*(3–4), 334–346. https://doi.org/10.1016/j.epsl.2010.08.004

Hergt, J. M., & Hawkesworth, C. J. (1994). Pb-, Sr-, and Nd-isotopic evolution of the Lau Basin: Implications for mantle dynamics during backarc opening. In J. W. Hawkins, L. M. Parson, J. F. Allan, N. Abrahamsen, U. Bednarz, G. Blanc, et al. (Eds.), *Proceedings of the Ocean Drilling Program, Scientific Results* (pp. 505–517).

Hirth, G., & Kohlstedt, D. L. (2003). Rheology of the upper mantle and the mantle wedge: A view from the experimentalists. In *Inside the subduction factory* (pp. 83–105). American Geophysical Union Geophysical Monograph.

Hofmann, A. W. (1988). Chemical differentiation of the Earth: The relationship between mantle, continental crust, and oceanic crust. *Earth and Planetary Science Letters*, *90*(3), 297–314. https://doi.org/10.1016/0012-821X(88)90132-X

Hofmann, A. W., Jochum, K. P., Seufert, M., & White, W. M. (1986). Nb and Pb in oceanic basalts: New constraints on mantle evolution. *Earth and Planetary Science Letters*, *79*(1–2), 33–45. https://doi.org/10.1016/0012-821x(86)90038-5

Jackson, M. G., Hart, S. R., Konter, J. G., Koppers, A. A. P., Staudigel, H., Kurz, M. D., et al. (2010). Samoan hot spot track on a "hot spot highway": Implications for mantle plumes and a deep Samoan mantle source. *Geochemistry, Geophysics, Geosystems*, *11*(12), Q12009. https://doi.org/10.1029/2010GC003232

Jarosevich, E. J., Nelen, J. A., & Norberg, J. A. (1980). Reference samples for electron microprobe analysis. *Geostandards Newsletter*, *4*(1), 43–47. https://doi.org/10.1111/j.1751-908X.1980.tb00273.x

Kelemen, P. B., Hirth, G., Shimizu, N., Spiegelman, M., & Dick, H. J. B. (1997). A review of melt migration processes in the adiabatically upwelling mantle beneath oceanic spreading ridges. *Philosophical Transactions of the Royal Society of London*, *A355*(1723), 283–318. https://doi.org/10.1098/rsta.1997.0010

Keller, N. S., Arculus, R. J., Hermann, J., & Richards, S. (2008). Submarine back-arc lava with arc signature: Fonualei Spreading Center, northeast Lau Basin, Tonga. *Journal of Geophysical Research*, *113*(B8). https://doi.org/10.1029/2007JB005451

Key, K., Constable, S., Liu, L., & Pommier, A. (2013). Electrical image of passive mantle upwelling beneath the northern East Pacific Rise. *Nature*, *495*(7442), 499–502. https://doi.org/10.1038/nature11932

Kim, J., Lee, K.-Y., & Kim, J.-H. (2011). Metal-bearing molten sulfur collected from a submarine volcano: Implications for vapor transport of metals in seafloor hydrothermal systems. *Geology*, *39*(4), 351–354. https://doi.org/10.1130/G31665.1

Konter, J. G., & Jackson, M. G. (2012). Large volumes of rejuvenated volcanism in Samoa: Evidence supporting a tectonic influence on late-stage volcanism. *Geochemistry, Geophysics, Geosystems*, *13*(6). https://doi.org/10.1029/2011GC003974

Kushiro, I. (2007). Origin of magmas in subduction zones: A review of experimental studies. *Proceedings of the Japan Academy*, *B83*, 1–15. https://doi.org/10.2183/pjab.83.1

Langmuir, C. H., Bézos, A., Escrig, S., & Parman, S. W. (2006). Chemical systematics and hydrous melting of the mantle in back-arc basins. In *Back-arc spreading systems: Geological, biological, chemical and physical interactions* (pp. 87–146). American Geophysical Union Geophysical Monograph.

Le Bas, M. J. (2000). IUGS reclassification of the high-Mg and picritic volcanic rocks. *Journal of Petrology*, *41*(10), 1467–1470. https://doi.org/10.1093/petrology/41.10.1467

Lima, S. M., Haase, K. M., Beier, C., Regelous, M., Brandl, P. A., Hauff, F., & Krumm, S. (2017). Magmatic evolution and source variations at the Nifonea Ridge (New Hebrides island arc). *Journal of Petrology*, *58*(3), 473–494. https://doi.org/10.1093/petrology/egx023

Lupton, J., Rubin, K. H., Arculus, R., Lilley, M., Butterfield, D., Resing, J., et al. (2015). Helium isotope, C/^{3}He, and Ba-Nb-Ti signatures in the northern Lau Basin: Distinguishing arc, back-arc, and hotspot affinities. *Geochemistry, Geophysics, Geosystems*, *16*(4), 1133–1155. https://doi.org/10.1002/2014GC005625

Lupton, J. E., Arculus, R. J., Greene, R. R., Evans, L. J., & Goddard, C. I. (2009). Helium isotope variations in seafloor basalts from the Northwest Lau Backarc Basin: Mapping the influence of the Samoan hotspot. *Geophysical Research Letters*, *36*(17), L17313. https://doi.org/10.1029/2009GL039468

McCulloch, M. T., & Gamble, J. A. (1991). Geochemical and geodynamical constraints on subduction zone magmatism. *Earth and Planetary Science Letters*, *102*(3–4), 358–374. https://doi.org/10.1016/0012-821X(91)90029-H

Michael, P. J. (1988). The concentration, behavior and storage of H_2O in the suboceanic upper mantle: Implications for mantle metasomatism. *Geochimica et Cosmochimica Acta*, *52*(2), 555–566. https://doi.org/10.1016/0016-7037(88)90110-X

Michael, P. J., & Cornell, W. C. (1998). Influence of spreading rate and magma supply on crystallization and assimilation beneath mid-ocean ridges: Evidence from chlorine and major element chemistry of mid-ocean ridge basalts. *Journal of Geophysical Research*, *103*(B8), 18325–18356. https://doi.org/10.1029/98JB00791

Millen, D. W., & Hamburger, M. W. (1998). Seismological evidence for tearing of the Pacific plate at the northern termination of the Tonga subduction zone. *Geology*, *26*(7), 659–662. https://doi.org/10.1130/0091-7613(1998)026<0659:SEFTOT>2.3.CO;2

Palacz, Z. A., & Saunders, A. D. (1986). Coupled trace element and isotopic enrichment in the Cook-Austral-Samoa islands, southwest Pacific. *Earth and Planetary Science Letters*, *79*(3–4), 270–280. https://doi.org/10.1016/0012-821X(86)90185-8

Park, J.-W., Campbell, I. H., Kim, J., & Moon, J.-W. (2015). The role of late sulfide saturation in the formation of a Cu- and Au-rich magma: Insights from the Platinum Group Element geochemistry of Niuatahi-Motutahi lavas, Tonga rear arc. *Journal of Petrology*, *56*(1), 59–81. https://doi.org/10.1093/petrology/egu071

Parman, S. W., & Grove, T. L. (2004). Harzburgite melting with and without H_2O: Experimental data and predictive modeling. *Journal of Geophysical Research*, *109*(B2). https://doi.org/10.1029/2003JB002566

Pearce, J. A., Ernewein, M., Bloomer, S. H., Parson, L. M., Murton, B. J., & Johnson, L. E. (1995). Geochemistry of Lau Basin volcanic rocks: Influence of ridge segmentation and arc proximity. In J. L. Smellie (Ed.), *Volcanism associated with extension at consuming plate margins* (pp. 53–75). Geological Society Special Publication.

Pearce, J. A., Kempton, P. D., & Gill, J. B. (2007). Hf-Nd evidence for the origin and distribution of mantle domains in the SW Pacific. *Earth and Planetary Science Letters*, *260*(1–2), 98–114. https://doi.org/10.1016/j.epsl.2007.05.023

Pearce, J. A., & Reagan, M. K. (2019). Identification, classification, and interpretation of boninites from Anthropocene to Eoarchean using Si-Mg-Ti systematics. *Geosphere*, *15*(4), 1008–1037. https://doi.org/10.1130/GES01661.1

Pearce, J. A., & Robinson, P. T. (2010). The Troodos ophiolitic complex probably formed in a subduction initiation, slab edge setting. *Gondwana Research*, *18*(1), 60–81. https://doi.org/10.1016/j.gr.2009.12.003

Pearce, J. A., & Stern, R. J. (2006). Origin of back-arc magmas: Trace element and isotope perspectives. In *Back-arc spreading systems: Geological, biological, chemical and physical interactions* (pp. 63–86). American Geophysical Union Geophysical Monograph Series.

Pearce, J. A., Stern, R. J., Bloomer, S. H., & Fryer, P. (2005). Geochemical mapping of the Mariana arc-basin system: Implications for the nature and distribution of subduction components. *Geochemistry, Geophysics, Geosystems*, *6*(7). https://doi.org/10.1029/2004GC000895

Pelletier, B., Calmant, S., & Pillet, R. (1998). Current tectonics of the Tonga-New Hebrides region. *Earth and Planetary Science Letters*, *164*(1–2), 263–276. https://doi.org/10.1016/S0012-821X(98)00212-X

Poreda, R. J., & Craig, H. (1992). He and Sr isotopes in the Lau Basin mantle: Depleted and primitive mantle components. *Earth and Planetary Science Letters*, *113*(4), 487–493. https://doi.org/10.1016/0012-821X(92)90126-G

Price, A. A., Jackson, M. G., Blichert-Toft, J., Blusztajn, J., Conatser, C. S., Konter, J. G., et al. (2016). Geochemical evidence in the northeast Lau Basin for subduction of the Cook-Austral volcanic chain in the Tonga Trench. *Geochemistry, Geophysics, Geosystems*, *17*(5), 1694–1724. https://doi.org/10.1002/2015gc006237

Price, A. A., Jackson, M. G., Blichert-Toft, J., Hall, P. S., Sinton, J. M., Kurz, M. D., & Blusztajn, J. (2014). Evidence for a broadly distributed Samoan-plume signature in the northern Lau and North Fiji Basins. *Geochemistry, Geophysics, Geosystems*, *15*(4), 986–1008. https://doi.org/10.1002/2013GC005061

Regelous, M., Collerson, K. D., Ewart, A., & Wendt, J. I. (1997). Trace element transport rates in subduction zones: Evidence from Th, Sr and Pb isotope data for Tonga-Kermadec arc lavas. *Earth and Planetary Science Letters*, *150*(3–4), 291–302. https://doi.org/10.1016/S0012-821X(97)00107-6

Resing, J. A., Rubin, K. H., Embley, R. W., Lupton, J. E., Baker, E. T., Dziak, R. P., et al. (2011). Active submarine eruption of boninite in the northeastern Lau Basin. *Nature Geoscience*, *4*(11), 799–806. https://doi.org/10.1038/ngeo1275

Romer, R. H. W., Beier, C., Haase, K. M., Klügel, A., & Hamelin, C. (2019). Progressive changes in magma transport at the active Serreta Ridge, Azores. *Geochemistry, Geophysics, Geosystems*, *20*(11), 5394–5414. https://doi.org/10.1029/2019GC008562

Ruellan, E., Delteil, J., Wright, I., & Matsumoto, T. (2003). From rifting to active spreading in the Lau Basin – Havre Trough backarc system (SW Pacific): Locking/unlocking induced by seamount chain subduction. *Geochemistry, Geophysics, Geosystems*, *4*(5), 8909. https://doi.org/10.1029/2001GC000261

Saunders, A. D., & Tarney, J. (1984). Geochemical characteristics of basaltic volcanism within back-arc basins. In B. P. Kokelaar & M. F. Howells (Eds.), *Marginal basin geology* (pp. 59–76). Geological Society of London Special Publication.

Schmeling, H. (2010). Dynamic models of continental rifting with melt generation. *Tectonophysics*, *480*(1–4), 33–47. https://doi.org/10.1016/j.tecto.2009.09.005

Sharaskin, A. Y., Karpenko, S. F., Ljalikov, A. V., Zlobin, S. K., & Balashov, Y. A. (1983). Correlated $^{143}Nd/^{144}Nd$ and $^{87}Sr/^{86}Sr$ data on boninites from Mariana and Tonga arcs. *Ofioliti*, *8*, 431–438.

Sleeper, J. D., & Martinez, F. (2014). Controls on segmentation and morphology along the back-arc Eastern Lau Spreading Center and Valu Fa Ridge. *Journal of Geophysical Research*, *119*(3), 1678–1700. https://doi.org/10.1002/2013JB010545

Smith, G. P., Wiens, D. A., Fischer, K. M., Dorman, L. M., Webb, S. C., & Hildebrand, J. A. (2001). A complex pattern of mantle flow in the Lau backarc. *Science*, *292*(5517), 713–716. https://doi.org/10.1126/science.1058763

Storch, B., Haase, K. M., Romer, R. H. W., Beier, C., & Koppers, A. A. P. (2020). Rifting of the oceanic Azores Plateau with episodic volcanic activity. *Scientific Reports*, *10*(1), 19718. https://doi.org/10.1038/s41598-020-76691-1

Stroncik, N. A., & Haase, K. M. (2004). Chlorine in oceanic intraplate basalts: Constraints on mantle sources and recycling processes. *Geology*, *32*(11), 945–948. https://doi.org/10.1130/G21027.1

Sun, S.-S., & McDonough, W. F. (1989). Chemical and isotopic systematics of oceanic basalts: Implications for mantle composition and processes. In A. D. Saunders & M. J. Norry (Eds.), *Magmatism in the ocean basins* (pp. 313–345). Geological Society, London, Special Publications.

Taylor, B. E., & Martinez, F. (2003). Back-arc basin basalt systematics. *Earth and Planetary Science Letters*, *210*(3–4), 481–497. https://doi.org/10.1016/S0012-821X(03)00167-5

Taylor, R. N., Ishizuka, O., Michalik, A., Milton, J. A., & Croudace, I. W. (2015). Evaluating the precision of Pb isotope measurement by mass spectrometry. *Journal of Analysis of Atomic Spectrometry*, *30*(1), 198–213. https://doi.org/10.1039/c4ja00279b

The MELT Seismic Team. (1998). Imaging the deep seismic structure beneath a mid-ocean ridge. *Science*, *280*(5367), 1215–1217. https://doi.org/10.1126/science.280.5367.1215

Thirlwall, M. F. (1991). Long-term reproducibility of multicollector Sr and Nd isotope ratio analysis. *Chemical Geology*, *94*(2), 85–104. https://doi.org/10.1016/S0009-2541(10)80021-X

Tian, L., Castillo, P. R., Hilton, D. R., Hawkins, J. W., Hanan, B. B., & Pietruszka, A. J. (2011). Major and trace element and Sr-Nd isotope signatures of the northern Lau Basin lavas: Implications for the composition and dynamics of the back-arc mantle. *Journal of Geophysical Research*, *116*(B11). https://doi.org/10.1029/2011JB008791

Turner, M., Ireland, T., Hermann, J., Holden, P., Padrón-Navarta, J. A., Hauri, E. H., & Turner, S. (2015). Sensitive high resolution ion microprobe–stable isotope (SHRIMP-SI) analysis of water in silicate glasses and nominally anhydrous reference minerals. *Journal of Analysis of Atomic Spectrometry*, *30*(8), 1706–1722. https://doi.org/10.1039/C5JA00047E

Turner, S., & Hawkesworth, C. (1998). Using geochemistry to map mantle flow beneath the Lau Basin. *Geology*, *26*(11), 1019–1022. https://doi.org/10.1130/0091-7613(1998)026<1019:UGTMMF>2.3.CO;2

Turner, S., Hawkesworth, C., Rogers, N., Bartlett, J., Worthington, T., Hergt, J., et al. (1997). ^{238}U-^{230}Th disequilibria, magma petrogenesis, and flux rates beneath the depleted Tonga-Kermadec island arc. *Geochimica et Cosmochimica Acta*, *61*(22), 4855–4884. https://doi.org/10.1016/S0016-7037(97)00281-0

Vervoort, J. D., & Blichert-Toft, J. (1999). Evolution of the depleted mantle: Hf isotope evidence from juvenile rocks through time. *Geochimica et Cosmochimica Acta*, *63*(3–4), 533–556. https://doi.org/10.1016/S0016-7037(98)00274-9

Volpe, A. M., Macdougall, J. D., & Hawkins, J. W. (1988). Lau Basin basalts (LBB): Trace element and Sr-Nd isotopic evidence for heterogeneity in backarc basin mantle. *Earth and Planetary Science Letters*, *90*(2), 174–186. https://doi.org/10.1016/0012-821X(88)90099-4

Wanless, V. D., & Behn, M. D. (2017). Spreading rate-dependent variations in crystallization along the global mid-ocean ridge system. *Geochemistry, Geophysics, Geosystems*, *18*(8), 3016–3033. https://doi.org/10.1002/2017GC006924

Wanless, V. D., Perfit, M. R., Ridley, W. I., Wallace, P. J., Grimes, C. B., & Klein, E. M. (2011). Volatile abundances and oxygen isotopes in basaltic to dacitic lavas on mid-ocean ridges: The role of assimilation at spreading centres. *Chemical Geology*, *287*(1–2), 54–65. https://doi.org/10.1016/j.chemgeo.2011.05.017

Wei, S. S., Zha, Y., Shen, W., Wiens, D. A., Conder, J. A., & Webb, S. C. (2016). Upper mantle structure of the Tonga-Lau-Fiji region from Rayleigh wave tomography. *Geochemistry, Geophysics, Geosystems*, *17*(11), 4705–4724. https://doi.org/10.1002/2016GC006656

Weis, D., Kieffer, B., Maerschalk, C., Barling, J., de Jong, J., Williams, G. A., et al. (2006). High-precision isotopic characterization of USGS reference materials by TIMS and MC-ICP-MS. *Geochemistry, Geophysics, Geosystems*, *7*(8), Q08006. https://doi.org/10.1029/2006GC001283

Weis, D., Kieffer, B., Maerschalk, C., Pretorius, W., & Barling, J. (2005). High-precision Pb-Sr-Nd-Hf isotopic characterization of USGS BHVO-1 and BHVO-2 reference materials. *Geochemistry, Geophysics, Geosystems*, *6*(2), Q02002. https://doi.org/10.1029/2004GC000852

Wendt, J. I., Regelous, M., Collerson, K. D., & Ewart, A. (1997). Evidence for a contribution from two mantle plumes to island-arc lavas from northern Tonga. *Geology*, *25*(7), 611–614. https://doi.org/10.1130/0091-7613(1997)025<0611:EFACFT>2.3.CO;2

Wiens, D. A., Kelley, K. A., & Plank, T. (2006). Mantle temperature variations beneath back-arc spreading centers inferred from seismology, petrology, and bathymetry. *Earth and Planetary Science Letters*, *248*(1–2), 30–42. https://doi.org/10.1016/j.epsl.2006.04.011

Woodhead, J., Eggins, S., & Gamble, J. (1993). High field strength and transition element systematics in island arc and back-arc basin basalts: Evidence for multi-phase melt extraction and a depleted mantle wedge. *Earth and Planetary Science Letters*, *114*(4), 491–504. https://doi.org/10.1016/0012-821X(93)90078-N

Workman, R. K., Hart, S. R., Jackson, M., Regelous, M., Farley, K. A., Blusztajn, J., et al. (2004). Recycled metasomatized lithosphere as the origin of the Enriched Mantle II (EM2) end-member: Evidence from the Samoan Volcanic Chain. *Geochemistry, Geophysics, Geosystems*, *5*(4), 2003GC000623. https://doi.org/10.1029/2003GC000623

Wright, E., & White, W. M. (1986). The origin of Samoa: New evidence from Sr, Nd, and Pb isotopes. *Earth and Planetary Science Letters*, *81*(2–3), 151–162. https://doi.org/10.1016/0012-821X(87)90152-X

Zellmer, K. E., & Taylor, B. (2001). A three-plate kinematic model for Lau Basin opening. *Geochemistry, Geophysics, Geosystems*, *2*(5), 2000GC000106. https://doi.org/10.1029/2000GC000106

Zindler, A., Staudigel, H., & Batiza, R. (1984). Isotope and trace element geochemistry of young Pacific seamounts: Implications for the scale of upper mantle heterogeneity. *Earth and Planetary Science Letters*, *70*(2), 175–195. https://doi.org/10.1016/0012-821X(84)90004-9